



1 **Nitrous Acid Budgets in Coastal Atmosphere: Insights into the Absence of a**  
2 **Daytime Marine Source**

3 Xuelian Zhong<sup>1</sup>, Hengqing Shen<sup>1\*</sup>, Min Zhao<sup>1</sup>, Ji Zhang<sup>1</sup>, Yue Sun<sup>1</sup>, Yuhong Liu<sup>1</sup>, Yingnan Zhang<sup>1</sup>,  
4 Ye Shan<sup>1</sup>, Hongyong Li<sup>1</sup>, Jiangshan Mu<sup>1</sup>, Yu Yang<sup>1</sup>, Yanqiu Nie<sup>1</sup>, Jinghao Tang<sup>2</sup>, Can Dong<sup>1</sup>, Xinfeng  
5 Wang<sup>1</sup>, Yujiao Zhu<sup>1</sup>, Mingzhi Guo<sup>2</sup>, Wenxing Wang<sup>1</sup>, and Likun Xue<sup>1\*</sup>

6 <sup>1</sup>Environment Research Institute, Shandong University, Qingdao, Shandong, 266237, China

7 <sup>2</sup>Collage of Mechanics and Materials, Hohai University, Nanjing, Jiangsu, 210098, China

8 *Correspondence to* Hengqing Shen (hqshen@sdu.edu.cn) and Likun Xue (xuelikun@sdu.edu.cn)

9

10 **Abstract.**

11 Nitrous acid (HONO), a vital precursor of atmospheric hydroxyl radicals (OH), has been extensively  
12 investigated to understand its characteristics and formation mechanisms. However, discerning  
13 fundamental mechanisms across diverse environments remains challenging. This study utilizes  
14 measurements from Mount Lao, a coastal mountain in eastern China, and an observation-based  
15 chemical box model to examine HONO budgets and their subsequent impacts on atmospheric  
16 oxidizing capacity. The model incorporates additional HONO sources, including direct emissions,  
17 heterogeneous conversions of NO<sub>2</sub> on aerosol and ground surfaces, and particulate nitrate photolysis.  
18 The observed mean HONO concentration was  $0.46 \pm 0.37$  ppbv. The updated model well reproduced  
19 daytime HONO concentrations during dust and photochemical pollution events. During dust events,  
20 daytime HONO formation was dominated by photo-enhanced heterogeneous reactions of NO<sub>2</sub> on  
21 aerosol surfaces (>50%), whereas particulate nitrate photolysis (34%) prevails during photochemical  
22 pollution events. Nevertheless, the model uncovers a significant unidentified marine HONO source in  
23 the “sea case”, with its HONO production rate reaching up to  $0.70$  ppbv h<sup>-1</sup> at noon. Without  
24 considering this unidentified source, an extraordinarily high photolysis coefficient of nitrate and/or  
25 heterogeneous uptake coefficient of NO<sub>2</sub> would be required to match observed HONO concentrations.  
26 This missing HONO source affected the peak O<sub>3</sub> production rate and OH radical concentration by 36%  
27 and 28%, respectively. Given the limited HONO observations data in coastal and marine settings, the  
28 unidentified HONO source may cause an underestimation of the atmosphere’s oxidizing capacity. This  
29 study highlights the necessity for further investigation of the role of HONO in atmospheric chemistry  
30 in coastal and marine environments.

31



## 32 **1 Introduction**

33 Atmospheric nitrous acid (HONO) serves as a pivotal precursor of hydroxyl radicals (OH)  
34 (Alicke et al., 2003), accounting for up to 60% of daytime OH radicals (Kleffmann et al., 2005; Czader  
35 et al., 2012). Thus, HONO establishes itself as a critical source of OH radical source in both urban and  
36 rural environments, surpassing the contribution from ozone (O<sub>3</sub>) photolysis (Elshorbany et al., 2012;  
37 Acker et al., 2006; Gu et al., 2022a). Consequently, HONO substantially influences the formation of  
38 secondary pollutants, including secondary aerosols and O<sub>3</sub>, exerting a considerable effect on air quality  
39 and climate change (Xing et al., 2019; Yang et al., 2021b).

40 Recent studies pinpoint four primary sources of atmospheric HONO: (a) Direct emissions from  
41 traffic (Liao et al., 2021), biomass burning (Nie et al., 2015; Theys et al., 2020), and soil (Su et al.,  
42 2011). (b) Homogeneous reaction of NO + OH, which is generally regarded as a significant process in  
43 polluted urban areas during daytime when NO and OH concentrations are relatively high (Gu et al.,  
44 2022a). (c) Heterogeneous reactions of NO<sub>2</sub> on various surfaces, such as mineral dust (Underwood et  
45 al., 2001), soil (Kebede et al., 2016), and aqueous surfaces (Wojtal et al., 2011). The uptake coefficient  
46 of NO<sub>2</sub>,  $\gamma(\text{NO}_2)$ , on these surfaces remains uncertain and is subject to varying factors, sparking debates  
47 regarding the importance of the heterogeneous conversion of NO<sub>2</sub> (Xue et al., 2022; Broske et al.,  
48 2003). (d) Photolysis of adsorbed nitric acid (HNO<sub>3</sub>) and particulate nitrate (pNO<sub>3</sub><sup>-</sup>), crucial  
49 contributors to daytime HONO formation (Gen et al., 2022; Ye et al., 2017), particularly in clean  
50 environments (Zhou et al., 2011; Ye et al., 2016a). However, HONO formation mechanisms in  
51 different environments remain contentious and require more detailed model evaluations (Jiang et al.,  
52 2022).

53 Over recent decades, the missing sources of daytime HONO have been extensively studied across  
54 diverse environments (Kleffmann, 2007; Jiang et al., 2022; Lee et al., 2016). However, our limited  
55 understanding of these unidentified HONO sources has hindered accurate assessments of atmospheric  
56 free radicals and oxidizing capacity (Tang et al., 2015). In areas with high concentrations of NO<sub>2</sub> and  
57 particulate matter, missing sources are often ascribed to the photolytic enhancement of heterogeneous  
58 NO<sub>2</sub> reactions (Su et al., 2008; Czader et al., 2012; Lee et al., 2016; Tong et al., 2016). Conversely, in  
59 remote areas, nitrate photolysis or soil emissions are perceived as significant contributors to daytime  
60 HONO sources (Cui et al., 2019; Ye et al., 2016a; Su et al., 2011). In polluted mountainous areas, the  
61 vertical transport of air masses may also contribute to observed daytime HONO concentrations (Jiang  
62 et al., 2020; Xue et al., 2022). During dust storms, the particle surface area increases sharply,  
63 potentially enhancing the heterogeneous reaction of NO<sub>2</sub>, yet the evaluations of dust impacts on  
64 daytime HONO are scarce (Wang, 2003). Overall, most existing HONO source studies lack



65 quantitative assessments based on models and fail to provide comparative analyses across different  
66 environmental scenarios.

67 Furthermore, recent observations of HONO in coastal and marine regions indicate the existence  
68 of marine HONO sources (Jiang et al., 2022; Crilley et al., 2021; Ye et al., 2016a; Yang et al., 2021a).  
69 The observed accelerated NO<sub>2</sub>-to-HONO conversion in marine air masses suggests that air-marine  
70 interactions enhance HONO production (Zha et al., 2014; Yang et al., 2021a). However, the  
71 heterogeneous conversion of NO<sub>2</sub> on vast air/water interface, a potential source of marine HONO,  
72 remains uncertain (Wojtal et al., 2011; Zhu et al., 2022; Yu et al., 2021). Nitrate Photolysis is believed  
73 to contribute to marine HONO sources (Ye et al., 2016a; Andersen et al., 2023), but significant  
74 controversy persists (Romer et al., 2018; Shi et al., 2021). The specific influencing factors remain  
75 unclear (Zhang et al., 2020; Andersen et al., 2023), with some studies suggesting other factors may be  
76 responsible (Yang et al., 2021a; Wojtal et al., 2011). However, most existing studies still rely on  
77 steady-state analysis, and there is a lack of quantitative research determining if current HONO  
78 mechanisms can adequately explain observed marine daytime HONO concentrations.

79 Mount Lao, located on the eastern coast of Qingdao, China, experiences influences from various  
80 air masses from the continent and the ocean. During the spring of 2021 (27 April–19 May), when dust  
81 and O<sub>3</sub> pollution occurred frequently, we conducted measurements on Mount Lao to explore the  
82 daytime HONO budgets in the coastal atmosphere. Utilizing the latest HONO formation mechanisms  
83 in the box model, we found that the existing parameters adequately accounted for the HONO sources  
84 during both dust and photochemical pollution periods. However, we identified a significant  
85 discrepancy between the simulated and observed HONO in the “sea case”. This discrepancy suggests  
86 that a substantial daytime source of marine-derived HONO is absent from the current chemical  
87 mechanisms. To compensate for this missing source, either an unprecedentedly large enhancement  
88 factor (EF) of nitrate photolysis or a heterogeneous uptake coefficient of NO<sub>2</sub> would be necessary if  
89 attributed solely to these known HONO sources.

## 90 **2 Methods**

### 91 **2.1 Field measurements**

92 Field measurements were conducted on the southeast coast of Mount Lao (36.15°N, 120.68°E,  
93 166 m above sea level) in Qingdao (Figure 1), approximately 1 km away from the Yellow Sea. The  
94 geographical location and elevation of Mount Lao make it an optimal location for examining the  
95 contrasts between marine and continental air masses and the chemical processes within the marine  
96 boundary layer. The relatively pristine condition of the area, coupled with minimal levels of



97 anthropogenic activities such as industrial emissions, establish Mount Lao as a representative of a  
98 clean environment. The field campaign was carried out during the spring of 2021 (27 April–19 May  
99 2021), a period when the air quality of Qingdao is often affected by dust storms from Mongolia and  
100 northwestern China, as well as by O<sub>3</sub> pollution. Consequently, the site at Mount Lao provides an  
101 opportune platform for investigating the fundamental formation mechanisms of HONO under diverse  
102 environmental conditions.

103 HONO was quantified using a water-based long-path absorption photometer (WLPAP, Beijing  
104 Zhichen Technology Co., Ltd, China). Ambient HONO was absorbed by deionized water alone, after  
105 which it reacted with a reagent comprising 3.44 g of sulfanilamide and 0.2 g of N-(1-naphthyl)-  
106 ethylenediamine-dihydrochloride (NED) in 10 liters of deionized water, leading to the formation of an  
107 azo dye. Two channels were employed to extract HONO and interfering gases, respectively. The  
108 absorbance of the azo dye was measured using a fiber optic spectrometer (USB 4000, Ocean Optics,  
109 USA) at both the measurement wavelength (550 nm) and the reference wavelength (580 nm). Regular  
110 automatic zero measurements using ultrapure nitrogen were conducted every two days to correct for  
111 baseline drift. The detection limit and detection ranges were 2 pptv and 5 pptv–2 ppmv, respectively.

112 A suite of commercial online analyzers monitored the concentrations of NO<sub>x</sub>, O<sub>3</sub>, SO<sub>2</sub>, and CO  
113 (42i, 49i, 43i, and 48i, respectively, Thermo Fisher Scientific Inc, USA). PM<sub>2.5</sub> was measured using a  
114 hybrid nephelometric/radiometric particulate mass monitor (SHARP-5030i, Thermo Fisher Scientific  
115 Inc, USA), while PM<sub>10</sub> mass data were obtained from the China National Environmental Monitoring  
116 Center (<https://quotsoft.net/air/>). During the field campaign, fifty-seven VOC canister samples were  
117 collected at 2-hour intervals from 9:00–19:00 local time on pollution episode days and at 6-hour  
118 intervals from 9:00–21:00 on non-episode days. These VOC samples were subsequently analyzed  
119 using gas chromatography and mass spectrometry (TT24xr, Markes, UK; GC–MS, Thermo Fisher  
120 Scientific Inc, USA) (Liu et al., 2021). A wide-range particle spectrometer (WPS, Model 1000XP,  
121 MSP, USA) was employed to determine the atmospheric particle number size distributions from 10  
122 nm to 10 μm. Taking into account the hygroscopic growth, the relative humidity-adjusted aerosol  
123 surface area concentration (Sa) was calculated based on the determined particle number size  
124 distributions. 95 offline particulate samples were collected every 3-hour interval from 7:00–19:00 and  
125 12-hour intervals from 19:00–7:00 utilizing a high-volume air-sampling system (TE-5170, Tisch  
126 Environmental Inc, USA). The inorganic compositions of the samples, including Cl<sup>-</sup>, NO<sub>3</sub><sup>-</sup>, SO<sub>4</sub><sup>-</sup>,  
127 NH<sub>4</sub><sup>+</sup>, Na<sup>+</sup>, K<sup>+</sup>, Mg<sup>2+</sup>, and Ca<sup>2+</sup>, were determined via ion chromatography (Dionex ICS-600, Thermo  
128 Fisher Scientific Inc, USA). Meteorological data, including temperature, RH, pressure, wind speed,  
129 and wind direction, were monitored by an ultrasonic integrated weather station (RS-FSXCS-N01-1).



130 This study distinguishes between the “sea case” and the “land case” by analyzing the backward  
131 trajectory of the air mass. Specifically, considering the short lifetime of HONO, the MeteoInfo model  
132 (Wang, 2012) was used to calculate 6-hour air mass backward trajectories starting at the height of 200  
133 meters above ground level, using meteorological parameters from the Global Data Assimilation  
134 System (GDAS, <ftp://arlftp.arlhq.noaa.gov/>). The criteria for differentiating between the “sea case”  
135 and “land case” is based on the time spent over land or sea during the 6-hour backward air mass, with  
136 cases that spent less than 1 hour over land designated as a “sea case” (Yang et al., 2021a). Following  
137 this criterion, we selected a total of 18 sea cases and 13 land cases (Table S1). The observation data  
138 for the “sea case” and the “land case” were averaged for subsequent analysis.

## 139 2.2 Model setup

140 An observation-based chemical box model (OBM) was employed to explore the HONO budgets  
141 and atmospheric oxidizing capacity. The chemical mechanism used for the modeling was obtained  
142 from the Master Chemical Mechanism (MCM) website (<http://mcm.york.ac.uk/>) and was based on the  
143 MCM v3.3.1 as proposed by Jenkin et al. (2015). The model was constrained with data including  
144 HONO, O<sub>3</sub>, NO, NO<sub>2</sub>, SO<sub>2</sub>, CO, VOCs, pNO<sub>3</sub><sup>-</sup>, Sa, temperature, RH, pressure, and JNO<sub>2</sub>. These  
145 variables were averaged and interpolated to a time resolution of 5 minutes, except for VOCs and pNO<sub>3</sub><sup>-</sup>  
146 which were recorded at 1-hour intervals. The calculation of the photolysis rate of NO<sub>2</sub>, JNO<sub>2</sub>, was  
147 determined using Equation 1:

$$JNO_2 = JNO_{2(TUV)} \times \frac{UV_{observed}}{UV_{TUV}} \quad (E1)$$

148 where JNO<sub>2(TUV)</sub> and UV<sub>TUV</sub> are obtained from the Tropospheric Ultraviolet and Visible (TUV)  
149 radiation model ([http://cprm.acom.ucar.edu/Models/TUV/Interactive\\_TUV/](http://cprm.acom.ucar.edu/Models/TUV/Interactive_TUV/)). The UV<sub>observed</sub> was  
150 obtained from the NASA GES DISC (<https://disc.gsfc.nasa.gov/>). Other photolysis frequencies were  
151 calculated in the OBM and scaled by JNO<sub>2</sub>. The time series of JNO<sub>2</sub> is presented in Figure S1. The  
152 model was pre-run for 1 day to stabilize the simulation of unconstrained species.

153 In the MCM v3.3.1, the formation of HONO is originally attributed to a homogeneous reaction,  
154 specifically NO + OH → HONO. This study extends the existing mechanism by incorporating  
155 additional sources of HONO into the chemical model. A description of these sources and their  
156 associated mechanisms is provided in the following, and the corresponding parameters are listed in  
157 Table 1.

## 158 Description of HONO sources and sinks adopted in the OBM

### 159 Direct emission



160 In the atmosphere, HONO can be directly released through the exhaust emissions of various  
161 sources. The HONO/NO<sub>x</sub> emission ratio, which typically averages around 0.8%, is a common  
162 parameter used to gauge the impact of these vehicular emissions on HONO concentration (Kleffmann  
163 et al., 2003). However, the ratio can fluctuate between 0.3% and 1.6%, depending on engine and fuel  
164 types (Kurtenbach et al., 2001). Prior research indicates that direct emissions contribute significantly  
165 to HONO concentration in urban settings (Zhang et al., 2019; Kramer et al., 2020). However, in rural  
166 and background areas, the vehicular contribution is comparatively insignificant (Liu et al., 2019b; Xue  
167 et al., 2022). Consequently, the contribution of vehicle emissions to HONO is not constant and varies  
168 based on the environment and traffic density.

#### 169 **Homogeneous reaction of OH + NO → HONO**



170 The reaction of NO + OH is considered an important gas-phase reaction for HONO formation,  
171 particularly during pollution periods when concentrations of NO and OH are high (Gu et al., 2022a).  
172 We employed the box model to calculate the reaction rate using complex rate coefficients from the  
173 MCM website (<http://mcm.york.ac.uk/parameters/complex.htm>).

#### 174 **Heterogeneous reaction of NO<sub>2</sub> on aerosol surfaces**



$$k_{\text{aerosol}} = 0.25 \times v_{\text{NO}_2} \times \text{Sa} \times \gamma_a \quad \gamma_a = 8 \times 10^{-6} \quad (\text{E2})$$

$$k_{\text{aerosol}, h\nu} = 0.25 \times v_{\text{NO}_2} \times \text{Sa} \times \gamma_{a, h\nu} \times \frac{J_{\text{NO}_2}}{J_{\text{NO}_2, \text{moon}}} \quad \gamma_{a, h\nu} = 4 \times 10^{-5} \quad (\text{E3})$$

$$v_{\text{NO}_2} = \sqrt{\frac{8RT}{\pi M}} \quad (\text{E4})$$

175 The heterogeneous conversion of NO<sub>2</sub> on surfaces is a significant source of HONO in the atmosphere.  
176 As illustrated by equations R2 and R3, NO<sub>2</sub> reacts with water and light on aerosol surfaces to produce  
177 HONO. The HONO formation rate from heterogeneous reactions is typically first-order with respect  
178 to NO<sub>2</sub> concentration (Aumont et al., 2003), and the reactivity of NO<sub>2</sub> is known to be significantly  
179 enhanced under irradiated conditions compared to darkness (Yu et al., 2022a). In this study, the uptake  
180 coefficients of NO<sub>2</sub> on the aerosol surface in dark and irradiated conditions,  $\gamma_a$  and  $\gamma_{a, h\nu}$ , were set to  
181  $8 \times 10^{-6}$  and  $4 \times 10^{-5}$  (Lelièvre et al., 2004; Vandenboer et al., 2013b), respectively. The molecular speed  
182 of NO<sub>2</sub> ( $v_{\text{NO}_2}$ , m s<sup>-1</sup>) was calculated using Equation 4, where R represents the ideal gas constant, 8.314  
183 J mol<sup>-1</sup> K<sup>-1</sup>, T is the absolute temperature (K), and M is the relative molecular weight of NO<sub>2</sub> (g mol<sup>-1</sup>



184 <sup>1</sup>).  $S_a$  is the surface area concentration ( $\text{m}^2 \text{m}^{-3}$ ) estimated from particle number concentrations  
 185 measured by the WPS.

186 **Heterogeneous reaction of NO<sub>2</sub> on ground surfaces**



$$k_{\text{ground}} = 0.25 \times V_{\text{NO}_2} \times \gamma_{\text{g}} \times \frac{S}{V} \quad \gamma_{\text{g}} = 1 \times 10^{-6} \quad (\text{E5})$$

$$k_{\text{ground}, h\nu} = 0.25 \times V_{\text{NO}_2} \times \gamma_{\text{g}, h\nu} \times \frac{S}{V} \times \frac{J_{\text{NO}_2}}{J_{\text{NO}_2, \text{noon}}} \quad \gamma_{\text{g}, h\nu} = 2 \times 10^{-5} \quad (\text{E6})$$

$$\frac{S}{V} = \frac{1.7}{\text{BLH}} \quad (\text{E7})$$

187 Equations 5 and 6 delineate the parameterizations for the heterogeneous reaction of NO<sub>2</sub> on the ground  
 188 surfaces, both in the absence and presence of light. The uptake coefficients of NO<sub>2</sub> on the ground  
 189 surface under dark and irradiated conditions,  $\gamma_{\text{g}}$  and  $\gamma_{\text{g}, h\nu}$ , respectively, were set to  $1 \times 10^{-6}$  and  $2 \times 10^{-5}$   
 190 (Kleffmann et al., 1998; Stemmler et al., 2006), respectively. Under ambient conditions, the relative  
 191 importance of gas uptake on ground and aerosol surfaces is uncertain, with the influence of land use  
 192 categories and chemical compositions (Li et al., 2019). The surface-to-volume ratio,  $\frac{S}{V}$ , is calculated  
 193 by an effective surface of 1.7 m<sup>2</sup> per geometric surface in Equation 7 (Vogel et al., 2003). Within the  
 194 model, the boundary layer height, BLH, is projected to increase from 300 m at dawn to 1500 m at  
 195 14:00 and then decrease back to 300 m at dusk (Xue et al., 2014).

196 **Photolysis of particulate nitrate**



$$k = \frac{J(\text{pNO}_3^-)}{J_{\text{HNO}_3, \text{noon}}} \times J_{\text{HNO}_3(\text{MCM})} \quad (\text{E8})$$

197 In Equation 8, the photolysis rate constant of gaseous HNO<sub>3</sub> at noon,  $J_{\text{HNO}_3, \text{noon}}$ , is chosen to be ~  
 198  $7 \times 10^{-7} \text{ s}^{-1}$  based on previous studies (Ye et al., 2016b).  $J_{\text{HNO}_3(\text{MCM})}$  is calculated by the box model.  
 199 Recent research has shown that the photolysis rate of particulate nitrate is significantly faster than that  
 200 in the gas and aqueous phases (Zhou et al., 2003; Ye et al., 2016a). We adopt a median value of  $8.3 \times 10^{-5}$   
 201  $\text{ s}^{-1}$  in our simulation based on a range provided by Ye et al. (2017). Considering the uncertainty of  
 202 the parameter values of the above-mentioned HONO formation mechanisms, we conducted the  
 203 sensitivity tests with lower and upper values in Sections 3.2 and 3.3.

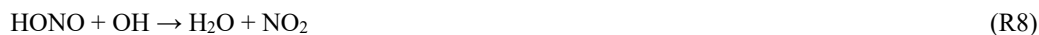
204 **Photolysis of HONO**





205 The primary loss pathway of HONO is through photolysis following sunrise, which significantly  
206 contributes to the atmospheric OH budget. The photolysis rate of HONO,  $J(\text{HONO})$ , in the OBM, is  
207 constrained by  $J\text{NO}_2$ .

#### 208 **Homogeneous reaction between HONO and OH**



209 The relevant kinetic parameter of the reaction between HONO and OH is available from the MCM  
210 mechanism, and its reaction rate coefficient is dependent solely on the temperature.

#### 211 **Dry deposition of HONO**

$$k = \frac{v_{\text{HONO}}}{\text{BLH}} \quad (\text{E9})$$

212 Here,  $v_{\text{HONO}}$  is the dry deposition velocity of HONO ( $\text{cm s}^{-1}$ ). Harrison and Kitto (1994) suggested the  
213 range of  $v_{\text{HONO}}$  was  $0.2\text{--}1.7 \text{ cm s}^{-1}$ , and a value of  $1.0 \text{ cm s}^{-1}$  was employed in this study.

### 214 **3 Results and discussion**

#### 215 **3.1 Concentration levels and temporal variations**

216 Figure 2 displays the time series of HONO, HONO/NO<sub>2</sub>, NO<sub>x</sub>, O<sub>3</sub>, CO, SO<sub>2</sub>, PM<sub>2.5</sub>, and pNO<sub>3</sub><sup>-</sup>,  
217 along with meteorological parameters (i.e., temperature, RH, and wind) measured throughout the field  
218 campaign. The presence of missing data in the time series resulted from instrument maintenance and  
219 calibration. Instrument maintenance and calibration resulted in gaps in the time series data. The  
220 observation site underwent dust periods on April 27–28 and May 7–8, as well as periods of  
221 photochemical pollution on May 5–6, 13, and 17–18. In this study, a photochemical pollution period  
222 is classified as a day when the maximum daily 8-hour average O<sub>3</sub> concentration (MDA8O<sub>3</sub>) exceeds  
223 75 ppbv (the Grade II National Ambient Air Quality Standard). A dust period is recognized when the  
224 peak PM<sub>10</sub> concentration surpasses  $150 \mu\text{g m}^{-3}$ , and the PM<sub>2.5</sub>/PM<sub>10</sub> ratio falls below 0.4, based on  
225 previous research (Liu et al., 2006; Wu et al., 2020). Section 3.2 provides a comprehensive explanation  
226 of the differences in pollutant concentrations and HONO budgets during dust and photochemical  
227 pollution periods.

228 Table 2 summarizes the descriptive statistics of the species and meteorological parameters  
229 measured during the observation period. The average ( $\pm$  standard deviation, SD) temperature and RH  
230 were  $15.1 \pm 3.4 \text{ }^\circ\text{C}$  and  $68.7 \pm 26.1\%$ , respectively, indicating a moderate spring temperature and  
231 relatively high RH influenced by marine air masses. The primary pollutant concentrations were  
232 relatively low, as indicated by the mean mixing ratios of  $0.9 \pm 1.7 \text{ ppbv}$ ,  $5.9 \pm 4.8 \text{ ppbv}$ ,  $284.0 \pm 118.8$   
233  $\text{ppbv}$ , and  $1.0 \pm 0.8 \text{ ppbv}$  for NO, NO<sub>2</sub>, CO, and SO<sub>2</sub>, respectively. These low levels suggest Mount





234 Lao is a relatively clean site with minimal impact from nearby anthropogenic sources. The high O<sub>3</sub>  
235 concentration ( $60.4 \pm 15.8$  ppbv) implies that photochemical reactions were relatively strong during  
236 observation. The mean concentrations of PM<sub>2.5</sub> and pNO<sub>3</sub><sup>-</sup> were  $21.2 \pm 21.09$   $\mu\text{g m}^{-3}$  and  $4.6 \pm 5.0$   $\mu\text{g}$   
237  $\text{m}^{-3}$ , respectively.

238 During the campaign, the mean concentration of HONO was  $0.46 \pm 0.37$  ppbv, with a maximum  
239 mixing ratio of 3.14 ppbv recorded at 17:00 on May 4th. The concentration level of HONO at Mount  
240 Lao is lower than at urban sites with higher NO<sub>2</sub> concentrations (Li et al., 2018; Yu et al., 2022b; Hao  
241 et al., 2020). However, it is notably higher than other clean coastal and remote marine sites, as Table  
242 S2 illustrates (Zhu et al., 2022; Zha et al., 2014; Meusel et al., 2016; Crilley et al., 2021; Villena et al.,  
243 2011). Past research conducted in urban and rural areas found that the HONO/NO<sub>2</sub> ratio, which  
244 indicates the extent of NO<sub>2</sub> conversion to HONO, typically ranges from 0.02 to 0.08 (Jiang et al., 2022).  
245 The higher HONO/NO<sub>2</sub> value (0.13) measured at Mount Lao highlights the potentially significant role  
246 of non-NO<sub>x</sub> related HONO sources or higher heterogeneous conversion of NO<sub>2</sub> efficiency at this site.

247 Figure 3 illustrates the average diurnal patterns of HONO and related species. The diurnal cycle  
248 of CO and SO<sub>2</sub> is similar, with peak concentrations observed during midday and relatively stable  
249 concentrations during nighttime. The concentration of O<sub>3</sub> increases with the accumulation of  
250 photochemical generation during the afternoon and decreases steadily after sunset. Contrary to most  
251 urban or rural locations, the concentration of HONO at Mount Lao peaks at noon, similar to remote  
252 areas (Jiang et al., 2022; Ye et al., 2016a). NO<sub>x</sub>, comprising NO and NO<sub>2</sub>, shows a similar temporal  
253 variation trend to HONO, suggesting potential photolytic sources for them (Reed et al., 2017). During  
254 the daytime (7:00–17:00), the average concentration of HONO was 1.56 times higher than at night  
255 (17:00–7:00), with concentrations of 0.54 ppbv during the day and 0.35 ppbv at night. Given the short  
256 lifetime of HONO during the day—only a matter of minutes—the noon HONO peak concentration  
257 suggests an in situ photochemical source for HONO (Kasibhatla et al., 2018). The ratio of HONO to  
258 NO<sub>2</sub> shows an increasing trend until sunrise, suggesting heterogeneous conversion from NO<sub>2</sub> to HONO  
259 during nighttime. However, unlike urban areas where the ratio of HONO to NO<sub>2</sub> decreases during the  
260 daytime (Zhang et al., 2019; Gu et al., 2022a), the ratio even increases during the midday period at  
261 Mount Lao, implying that HONO from sources other than NO<sub>2</sub> conversion also significantly  
262 contributes to HONO concentration (Yang et al., 2021a). Considering that the influence of HONO on  
263 the OH radical and O<sub>3</sub> is primarily observed during the daytime, the higher concentration of HONO  
264 during the daytime at the Mount Lao site suggests the presence of strong daytime HONO sources. The  
265 primary objective of our following study is to analyze the daytime budgets of HONO in the coastal  
266 atmosphere of Mount Lao.



### 267 3.2 Daytime HONO budgets in dust and photochemical pollution periods

268 The daytime HONO budgets were examined during periods of dust and photochemical pollution  
269 using an updated OBM, with the aim of assessing whether our current understanding of HONO sources  
270 is sufficient to explain observed concentrations. Table 4 presents the mean daytime concentrations of  
271 HONO and other species during the dust, photochemical pollution, and non-polluted periods (i.e., days  
272 devoid of dust and photochemical pollution). On average, the daytime HONO concentrations during  
273 dust and photochemical pollution periods were  $0.57 \pm 0.39$  ppbv and  $0.44 \pm 0.29$  ppbv, respectively.  
274 The dust period exhibited significantly higher concentrations of  $\text{NO}_2$ ,  $\text{PM}_{2.5}$ ,  $\text{pNO}_3^-$ , and Sa, with  
275 increased factors of 1.4, 2.6, 2.3, and 2.3, respectively, compared to the non-polluted period. During  
276 the photochemical pollution period, the daytime mean values of  $\text{O}_3$ , CO,  $\text{SO}_2$ ,  $\text{PM}_{2.5}$ ,  $\text{pNO}_3^-$ , and  $\text{JNO}_2$   
277 were 78.8 ppbv, 353.8 ppbv, 1.7 ppbv,  $25.0 \mu\text{g m}^{-3}$ ,  $6.2 \mu\text{g m}^{-3}$ , and  $7.0 \times 10^{-3} \text{ s}^{-1}$ , respectively. These  
278 values were approximately 1.4, 1.3, 2.4, 1.5, 2.1, and 1.6 times higher than those during the non-  
279 polluted period.

280 Figure 4 compares the observed and modeled HONO concentrations during dust and  
281 photochemical pollution periods and illustrates the contribution of various sources and sinks to the  
282 HONO budget. The study examined two scenarios: the base case, which only considered the  
283 homogeneous reaction  $\text{NO} + \text{OH}$ , and the model case, which considered all seven HONO sources  
284 outlined in Table 1. The results indicated that the base case significantly underestimated the HONO  
285 concentration, consistent with previous studies (Liu et al., 2019b; Zhu et al., 2022). However, the  
286 model case effectively replicated the observed HONO concentrations for both periods, even the high  
287 noon concentrations. The index of agreement (IOA) values for HONO during the dust and  
288 photochemical pollution periods were 0.96 and 0.88, respectively. This suggests that the updated  
289 parameterization scheme employed in the model can adequately account for the observed HONO  
290 concentrations at Mount Lao.

291 During the daytime, the average modeled production rates of HONO were  $1.66 \text{ ppbv h}^{-1}$  and  $0.90$   
292  $\text{ppbv h}^{-1}$  for the dust and photochemical pollution periods, respectively. The maximum HONO  
293 production rate was significantly higher during the dust period ( $3.50 \text{ ppbv h}^{-1}$ ) compared to the  
294 photochemical pollution period ( $1.69 \text{ ppbv h}^{-1}$ ) and was even comparable to levels observed during  
295 haze periods at polluted urban or rural sites (Xue et al., 2020; Gu et al., 2022a; Zhang et al., 2019).

296 Based on the model results of detailed HONO budgets, the dominant pathway for daytime HONO  
297 production during the dust period was photo-enhanced heterogeneous conversion of  $\text{NO}_2$  on the  
298 aerosol surface, accounting for 53% ( $0.87 \pm 0.66 \text{ ppbv h}^{-1}$ ) of the simulated daytime HONO production



299 rate. Wang (2003) reported sudden increases in HONO concentration during nocturnal dust storm  
300 events and observed a higher ratio of HONO to NO<sub>2</sub> (0.18). The enhanced efficiency of NO<sub>2</sub> to HONO  
301 on mineral dust particles suggests a potentially significant impact of dust aerosol on nitrogen  
302 compound distribution. Further research is needed to understand the contribution of dust to HONO  
303 formation and nitrogen cycling during the daytime, as well as its global impact. For the photochemical  
304 pollution period, the major sources of HONO included the photolysis of particulate nitrate, the photo-  
305 enhanced heterogeneous conversion of NO<sub>2</sub> on the aerosol surface, and the homogeneous reaction of  
306 OH and NO, which contributed 34%, 27%, and 27% of the daytime HONO production rate,  
307 respectively. This points to the significant role of photochemical processes under intense solar radiation.  
308 Direct emissions had a negligible contribution during both the dust and photochemical pollution  
309 periods, accounting for less than 2%. The photolysis of HONO was the dominant loss pathway  
310 throughout the day for all measurement periods, accounting for more than 90% of HONO sinks.

311 The model was subjected to sensitivity tests by increasing or decreasing selected parameters by  
312 factors of 5 and 2 (Table S4, Figures S2, and S3). Even with such a broad range of parameter variation,  
313 the heterogeneous reaction of NO<sub>2</sub> on aerosols and the photolysis of nitrate to form atmospheric HONO  
314 remained significant sources of HONO under both dust and photochemical pollution periods. This  
315 suggests that our current understanding of HONO sources, based on existing mechanisms, can  
316 generally explain the observed concentrations of HONO. However, it is important to note that  
317 differences in parameter selection can significantly affect the relative contributions of each pathway.  
318 Given the considerable uncertainties in the uptake coefficient of NO<sub>2</sub> and the enhancement factors of  
319 photolysis of nitrate, further experimental studies are necessary to evaluate their effects on HONO in  
320 different environmental conditions.

### 321 **3.3 Missing daytime HONO source in “sea case”**

322 Recent field studies suggest potential unidentified daytime sources of nitrous acid (HONO) in the  
323 marine atmosphere, with high daytime HONO levels recorded (Yang et al., 2021a; Ye et al., 2016a).  
324 Figure 5 shows the diurnal variation of the selected “sea case” and “land case”, with corresponding  
325 statistical results in Table S3. In the “sea case”, daytime concentrations of typical primary pollutants,  
326 such as CO and SO<sub>2</sub>, are significantly lower than those in the “land case” (251 ± 59 ppbv vs. 335 ±  
327 115 ppbv and 0.7 ± 0.4 ppbv vs. 1.4 ± 0.8 ppbv for CO and SO<sub>2</sub>, respectively). Concurrently, the “sea  
328 case” shows a lower daytime temperature (15.2 ± 3.0°C vs. 18.7 ± 3.8°C) and higher RH (76.3 ± 25.9%  
329 vs. 47.3 ± 20.3%) compared to the “land case”. This is consistent with our understanding of marine air  
330 masses, which tend to be cleaner and more humid. These findings validate our classification method  
331 of “land case” and “sea case” based on the backward air mass trajectory.



332 Secondary pollutants in marine air masses, such as  $O_3$ ,  $PM_{2.5}$ , and  $pNO_3^-$ , also register lower  
333 daytime concentrations than in the “land case” ( $59.4 \pm 10.3$  ppbv vs.  $63.4 \pm 13.3$  ppbv,  $13.2 \pm 5.8$   $\mu g$   
334  $m^{-3}$  vs.  $29.9 \pm 22.8$   $\mu g m^{-3}$ , and  $1.3 \pm 0.5$   $\mu g m^{-3}$  vs.  $10.0 \pm 3.3$   $\mu g m^{-3}$ , respectively). Though the  
335 HONO concentration in marine air masses is less than that in the “land case” ( $0.42 \pm 0.25$  ppbv vs.  
336  $0.51 \pm 0.22$  ppbv), it maintains a relatively high level, particularly during intense photolysis periods  
337 around noon when the HONO concentration in the “sea case” marginally increases.  $NO_x$   
338 concentrations in the “sea case” are also lower than in the “land case”, but the difference is less  
339 substantial than primary pollutants, with both NO and  $NO_2$  showing concentration peaks around noon.  
340 Nighttime observations in the “sea case” show a higher HONO/ $NO_2$  ratio (0.12), which has been noted  
341 in earlier studies (Zha et al., 2014), suggesting strong nocturnal HONO formation in marine air masses.  
342 Here, we focus on the sources of HONO during the day under the influence of marine air masses.

343 Utilizing the updated chemical model, we examine the HONO budgets in both “sea” and “land” cases.  
344 In the “land case”, the simulated HONO concentration aligns well with the observed HONO  
345 concentration, with a high index of agreement (IOA) value of 0.94 (Figure 6a). The peak HONO  
346 production rate observed at Mount Lao ( $2.69$  ppbv  $h^{-1}$ ) surpasses that calculated in continental air  
347 masses at Hok Tsui, Hong Kong (less than  $1.5$  ppbv  $h^{-1}$ ) (Gu et al., 2022b). The contributions of photo-  
348 enhanced heterogeneous reactions of  $NO_2$  on the aerosol surface (22%) and photolysis of  $pNO_3^-$  (20%)  
349 are comparable (Figure 6c). Model results reveal that the homogeneous reaction between NO and OH  
350 is the predominant HONO formation pathway, contributing an average of 44% ( $0.52 \pm 0.38$  ppbv  $h^{-1}$ ).  
351 Despite a lower absolute rate than in urban areas, the relative contribution is significant (Gu et al.,  
352 2022a; Yu et al., 2022b). This result suggests that similar to the findings in the cases of dust and  
353 photochemical pollution, the current model’s parameterization reasonably accounts for the observed  
354 HONO concentration in the “land case”.

355 However, in the “sea case”, while the updated model has improved in simulating HONO  
356 concentrations, with an average concentration increase from 0.05 ppbv to 0.11 ppbv, it falls short of  
357 the observed concentration (0.42 ppbv), indicating a substantial unidentified HONO source. At noon,  
358 the missing HONO production rate ( $P_{missing}$ ) can reach up to  $0.70$  ppbv  $h^{-1}$ . This value is slightly higher  
359 than the result calculated by Meusel et al. (2016) on Cyprus Island (about  $0.5$  ppbv  $h^{-1}$ ), but lower than  
360 that reported by Yang et al. (2021a) in coastal Qingdao (up to  $1.83$  ppbv  $h^{-1}$ , including all non-NO+OH  
361 pathways). Sensitivity tests were conducted to assess the impact of parameter selection on simulation  
362 results, but even with much larger parameters (Table S4), the model fails to explain the observed  
363 HONO concentrations (Figure S4).



364 The correlation analysis reveals that the missing HONO production rate correlates strongly with  
365  $JNO_2$  and  $JNO_2 \times pNO_3^-$  (Figure S6), with correlation coefficients ( $r$ ) of 0.90 and 0.73, respectively.  
366 This indicates that the missing HONO sources are closely related to photochemical processes. This  
367 concurs with recent multi-site HONO analysis results, which propose a significant role of  
368 photochemical processes in observed HONO concentrations in remote areas (Jiang et al., 2022). We  
369 postulate that all missing HONO originates from photochemical processes and have calculated the  
370 required enhancement factors (EF) for nitrate photolysis rates (Text S2) and the uptake coefficient  
371 required for  $NO_2$  on aerosol and ground surfaces (Figure S5). To account for the observed HONO  
372 concentrations, the required EF is approximately 4000. While Andersen et al. (2023) noted that the EF  
373 increases with decreasing nitrate concentration, a 4000-fold difference exceeds all laboratory and field  
374 observations to date (Ye et al., 2017; Andersen et al., 2023). The required uptake coefficient of  $NO_2$   
375 on aerosol and ground surface reach  $4 \times 10^{-4}$ , exceeding previous laboratory studies (Liu et al., 2019a;  
376 Stemmler et al., 2007). This suggests that the observed missing HONO source in the “sea case” cannot  
377 be explained by the current photochemical processes. This deviates from the findings of Zhu et al.  
378 (2022), who discovered that nitrate photolysis could explain the observed HONO concentrations in  
379 clean marine air masses using a moderate EF of 29. In recent years, many observations have noted  
380 distinct HONO characteristics under the influence of marine air masses, differing from those in  
381 continental air masses, but the specific mechanisms are still lacking (Yang et al., 2021a; Zhu et al.,  
382 2022; Crilley et al., 2021; Meusel et al., 2016). The ocean surface contains abundant nitrogen-  
383 containing substances (e.g., dissolved nitrate, ammonia, aliphatic amine, dissolved free amino acids)  
384 (Donaldson and George, 2012; Altieri et al., 2016), encompassing both organic and inorganic nitrogen.  
385 This is particularly true in polluted coastal areas where surface nitrogen content is rich. It merits  
386 investigation whether these nitrogen-containing substances in the alkaline sea-surface microlayer can  
387 directly affect HONO production or enhance HONO formation by photolysis on the formed sea salt  
388 aerosols. Additionally, the presence of halogens in oceanic air masses might promote nitrate photolysis  
389 (Zhang et al., 2020).

### 390 **3.4 Impacts of HONO on $O_3$ and OH production**

391 To quantify the impact of HONO, especially in the marine atmosphere, on  $O_3$  and OH radicals,  
392 we conducted further scenario simulations using a chemical box model. In the “with HONO” scenario,  
393 we input the observed HONO concentrations to constrain the model. In contrast, in the “without  
394 HONO” scenario, the model set HONO concentrations to zero. The differences between these  
395 scenarios illustrate the impact of HONO chemistry on  $O_3$  and OH radicals in the atmosphere. To further  
396 investigate the effect of the missing HONO sources in marine air masses, we established a third



397 simulation scenario, “without missing HONO”, in the marine air mass simulation. In this scenario, the  
398 model includes the latest HONO formation mechanisms discussed earlier but without the constraint of  
399 observed HONO.

400 HONO significantly influences the production of O<sub>3</sub> and OH radicals, regardless of whether the  
401 overall situation during the observation period (“overall case”) or the situation within the marine air  
402 masses (“sea case”) is considered (Figure 7). The net O<sub>3</sub> production rate can be determined by the  
403 difference between the O<sub>3</sub> production rate (P(O<sub>3</sub>)) and loss rate (L(O<sub>3</sub>)) (Xue et al., 2014). Specifically,  
404 the absence of HONO resulted in a decrease in the O<sub>3</sub> and OH radical production rates in the “overall  
405 case” from 7.39 ppbv h<sup>-1</sup> and 1.44×10<sup>7</sup> molecules cm<sup>-3</sup> s<sup>-1</sup> to 2.99 ppbv h<sup>-1</sup> (a 59% reduction) and  
406 2.78×10<sup>6</sup> molecules cm<sup>-3</sup> s<sup>-1</sup> (an 81% reduction), respectively. Similarly, in the marine air masses, the  
407 O<sub>3</sub> and OH radical production rates decreased from 6.22 ppbv h<sup>-1</sup> and 7.69×10<sup>6</sup> molecules cm<sup>-3</sup> s<sup>-1</sup> to  
408 3.20 ppbv h<sup>-1</sup> (a 49% reduction) and 2.11×10<sup>6</sup> molecules cm<sup>-3</sup> s<sup>-1</sup> (a 73% reduction), respectively.  
409 Regarding concentration, the absence of HONO chemistry resulted in a reduction in the average O<sub>3</sub>  
410 concentration in the overall situation from 40.4 ppbv to 35.0 ppbv and a reduction in the average OH  
411 radical concentration from 3.6×10<sup>6</sup> molecules cm<sup>-3</sup> to 1.7×10<sup>6</sup> molecules cm<sup>-3</sup>. Furthermore, the peak  
412 concentrations of O<sub>3</sub> and OH radicals decreased by 15% and 53% (from 59.3 ppbv to 50.3 ppbv and  
413 from 5.2×10<sup>6</sup> molecules to 2.4×10<sup>6</sup> molecules cm<sup>-3</sup>), respectively. These findings are consistent with  
414 previous observational studies (Gu et al., 2022a; Yang et al., 2021a), highlighting the significant  
415 impact of HONO on O<sub>3</sub> and OH radicals.

416 The simulated O<sub>3</sub> and OH radical concentrations for marine air masses also significantly decrease  
417 when the missing HONO source is not considered (“without missing HONO”). Specifically, the  
418 average O<sub>3</sub> concentration decreased from 29.1 ppbv to 26.8 ppbv (an 8% reduction), while the average  
419 OH radical concentration decreased from 2.5×10<sup>6</sup> molecules cm<sup>-3</sup> to 1.8×10<sup>6</sup> molecules cm<sup>-3</sup> (a 30%  
420 reduction). The peak concentrations of O<sub>3</sub> and OH radicals decreased by 8% and 28% (from 40.8 ppbv  
421 to 37.4 ppbv and from 3.4×10<sup>6</sup> molecules cm<sup>-3</sup> to 2.4×10<sup>6</sup> molecules cm<sup>-3</sup>), respectively. Regarding  
422 the relative contribution to OH radicals, HONO accounts for 79% and 55% in the “overall case” and  
423 “sea case”, respectively, both exceeding the combined contribution of other pathways (photolysis of  
424 O<sub>3</sub> contributes 14% and 25%, respectively). Notably, in the “sea case”, if the observed values are not  
425 input as constraints, and only the updated mechanisms are used, the model still significantly  
426 underestimates the impact of HONO on O<sub>3</sub> and OH radicals. Given the relatively limited observational  
427 data on HONO in coastal or marine areas and the unclear understanding of the missing HONO sources  
428 in the ocean, the impact of marine emissions on atmospheric oxidizing capacity may be significantly



429 underestimated. This underscores the importance of further research in this area to enhance our  
430 understanding of the role of HONO in atmospheric chemistry, especially in marine environments.

#### 431 **4 Conclusions**

432 This study presents a comprehensive investigation of the characteristics and sources of nitrous  
433 acid (HONO) in the coastal environment of Qingdao. The analysis utilizes observational data from the  
434 Mount Lao site in Qingdao during spring 2021 and an updated chemical box model that integrates  
435 HONO mechanisms. The focus lies on discerning the unidentified HONO sources in marine air masses  
436 and comprehending their effects on atmospheric chemistry, emphasizing O<sub>3</sub> and OH concentrations.

437 Despite a relatively pristine coastal atmosphere, HONO concentrations are considerably higher  
438 than previously thought ( $0.46 \pm 0.37$  ppbv), notably during daytime. This observation persists in lower  
439 primary pollutant concentrations such as CO and SO<sub>2</sub> within marine air masses, suggesting missing  
440 HONO sources tied to photochemical processes. An updated chemical model's simulation reveals that  
441 the mechanisms behind HONO formation can satisfactorily account for the observed HONO  
442 concentrations during the dust and photochemical pollution periods. Yet, in marine scenarios, the  
443 model falls short of matching observed concentrations, pointing to a strong unidentified HONO source  
444 within the marine atmosphere. Sensitivity tests and correlation analyses emphasize the importance of  
445 photochemical processes in unidentified HONO sources. Nevertheless, if these unknown sources are  
446 attributed to either nitrate photolysis or heterogeneous NO<sub>2</sub> reactions, the necessary nitrate photolysis  
447 rate and the heterogeneous uptake coefficient of NO<sub>2</sub> would surpass the upper thresholds established  
448 by current laboratory studies. In light of these findings, future research must target uncovering the  
449 mechanisms behind the missing HONO sources in marine air masses. Specifically, the role of nitrogen-  
450 containing substances at the ocean's surface and the potential influence of halogens in promoting  
451 nitrate photolysis warrant further examination.

452



453 **Acknowledgments**

454 This work was supported by the National Natural Science Foundation of China (grants nos.  
455 42061160478 and 42105106) and the National Key Research and Development Programme of the  
456 Ministry of Science of Technology of China (grant no. 2022YFC3701101). We would like to express  
457 our gratitude to the University of Leeds for providing the Master Chemical Mechanism and to NCAR  
458 for the Tropospheric Ultraviolet Visible (TUV) radiation model. We also thank Yaqiang Wang for  
459 developing the open-source software MeteoInfo.

460 **Author contributing**

461 LX and HS conceptualized the research. XZ drafted the initial manuscript and analyzed the data. CD  
462 supported funding the observation. YZ, CD, and XW designed the field campaign. MZ, JZ, YS, YL,  
463 YS, HL, and JM conducted the field campaign. JZ and YL analyzed the aerosol samples and VOC  
464 samples, respectively. MZ and YZ assisted with the model simulation. YY, YN, and JT contributed to  
465 figure creation. LX, HS, MG, and WW revised the original manuscript.

466 **Competing interests**

467 The authors declare that they have no conflict of interest.

468 **Data availability**

469 The data supporting this study are available upon request from the corresponding author.

470





471 **References**

- 472 Acker, K., Möller, D., Wieprecht, W., Meixner, F. X., Bohn, B., Gilge, S., Plass-Dülmer, C., and  
473 Berresheim, H.: Strong daytime production of OH from HNO<sub>2</sub> at a rural mountain site,  
474 *Geophys. Res. Lett.*, 33, 4, <https://doi.org/10.1029/2005GL024643>, 2006.
- 475 Aliche, B., Geyer, A., Hofzumahaus, A., Holland, F., Konrad, S., Pätz, H. W., Schäfer, J., Stutz, J.,  
476 Volz-Thomas, A., and Platt, U.: OH formation by HONO photolysis during the BERLIOZ  
477 experiment, *J. Geophys. Res. Atmos.*, 108, PHO 3-1-PHO 3-17,  
478 <https://doi.org/10.1029/2001JD000579>, 2003.
- 479 Altieri, K. E., Fawcett, S. E., Peters, A. J., Sigman, D. M., and Hastings, M. G.: Marine biogenic source  
480 of atmospheric organic nitrogen in the subtropical North Atlantic, *Proc. Natl. Acad. Sci.*, 113,  
481 925-930, <https://doi.org/10.1073/pnas.1516847113>, 2016.
- 482 Andersen, S. T., Carpenter, L. J., Reed, C., Lee, J. D., Chance, R., Sherwen, T., Vaughan, A. R.,  
483 Stewart, J., Edwards, P. M., Bloss, W. J., Sommariva, R., Crilley, L. R., Nott, G. J., Neves, L.,  
484 Read, K., Heard, D. E., Seakins, P. W., Whalley, L. K., Boustead, G. A., Fleming, L. T., Stone,  
485 D., and Fomba, K. W.: Extensive field evidence for the release of HONO from the photolysis  
486 of nitrate aerosols, *Science Advances*, 9, <https://doi.org/10.1126/sciadv.add6266>, 2023.
- 487 Aumont, B., Chervier, F., and Laval, S.: Contribution of HONO sources to the NO<sub>x</sub>/HO<sub>x</sub>/O<sub>3</sub> chemistry  
488 in the polluted boundary layer, *Atmos. Environ.*, 37, 487-498, [https://doi.org/10.1016/S1352-2310\(02\)00920-2](https://doi.org/10.1016/S1352-2310(02)00920-2), 2003.
- 490 Bröske, R., Kleffmann, J., and Wiesen, P.: Heterogeneous conversion of NO<sub>2</sub> on secondary organic  
491 aerosol surfaces: A possible source of nitrous acid (HONO) in the atmosphere?, *Atmos. Chem.  
492 Phys.*, 3, 469-474, <https://doi.org/10.5194/acp-3-469-2003>, 2003.
- 493 Crilley, L. R., Kramer, L. J., Pope, F. D., Reed, C., Lee, J. D., Carpenter, L. J., Hollis, L. D. J., Ball,  
494 S. M., and Bloss, W. J.: Is the ocean surface a source of nitrous acid (HONO) in the marine  
495 boundary layer?, *Atmos. Chem. Phys.*, 21, 18213–18225, <https://doi.org/10.5194/acp-21-18213-2021>, 2021.
- 497 Cui, L. L., Li, R., Fu, H. B., Li, Q., Zhang, L. W., George, C., and Chen, J. M.: Formation features of  
498 nitrous acid in the offshore area of the East China Sea, *Sci. Total Environ.*, 682, 138-150,  
499 <https://doi.org/10.1016/j.scitotenv.2019.05.004>, 2019.
- 500 Czader, B. H., Rappenglück, B., Percell, P., Byun, D. W., Ngan, F., and Kim, S.: Modeling nitrous  
501 acid and its impact on ozone and hydroxyl radical during the Texas Air Quality Study 2006,  
502 *Atmos. Chem. Phys.*, 12, 6939–6951, <https://doi.org/10.5194/acp-12-6939-2012>, 2012.
- 503 Donaldson, D. J. and George, C.: Sea-Surface Chemistry and Its Impact on the Marine Boundary Layer,  
504 *Environ. Sci. Technol.*, 46, 10385-10389, <https://doi.org/10.1021/es301651m>, 2012.
- 505 Elshorbany, Y. F., Steil, B., Brühl, C., and Lelieveld, J.: Impact of HONO on global atmospheric  
506 chemistry calculated with an empirical parameterization in the EMAC model, *Atmos. Chem.  
507 Phys.*, 12, 9977–10000, <https://doi.org/10.5194/acp-12-9977-2012>, 2012.
- 508 Gen, M., Liang, Z., Zhang, R., Go Mabato, B. R., and Chan, C. K.: Particulate nitrate photolysis in the  
509 atmosphere, *Environ. Sci.: Atmos.*, <https://doi.org/10.1039/D1EA00087J>, 2022.
- 510 Gu, R., Shen, H., Xue, L., Wang, T., Gao, J., Li, H., Liang, Y., Xia, M., Yu, C., Liu, Y., and Wang,  
511 W.: Investigating the sources of atmospheric nitrous acid (HONO) in the megacity of Beijing,  
512 China, *Sci. Total Environ.*, 812, 152270, <https://doi.org/10.1016/j.scitotenv.2021.152270>,  
513 2022a.
- 514 Gu, R., Wang, W., Peng, X., Xia, M., Zhao, M., Zhang, Y., Wang, Y. n., Liu, Y., Shen, H., Xue, L.,  
515 Wang, T., and Wang, W.: Nitrous acid in the polluted coastal atmosphere of the South China  
516 Sea: Ship emissions, budgets, and impacts, *Sci. Total Environ.*, 826, 153692,  
517 <https://doi.org/10.1016/j.scitotenv.2022.153692>, 2022b.
- 518 Hao, Q., Jiang, N., Zhang, R., Yang, L., and Li, S.: Characteristics, sources, and reactions of nitrous  
519 acid during winter at an urban site in the Central Plains Economic Region in China, *Atmos.  
520 Chem. Phys.*, 20, 7087–7102, <https://doi.org/10.5194/acp-20-7087-2020>, 2020.



- 521 Harrison, R. M. and Kitto, A.-M. N.: Evidence for a surface source of atmospheric nitrous acid, *Atmos.*  
522 *Environ.*, 28, 1089-1094, [https://doi.org/10.1016/1352-2310\(94\)90286-0](https://doi.org/10.1016/1352-2310(94)90286-0), 1994.
- 523 Jenkin, M. E., Young, J. C., and Rickard, A. R.: The MCM v3.3.1 degradation scheme for isoprene,  
524 *Atmos. Chem. Phys.*, 15, 11433–11459, <https://doi.org/10.5194/acp-15-11433-2015>, 2015.
- 525 Jiang, Y., Xue, L. K., Shen, H. Q., Dong, C., Xiao, Z. S., and Wang, W. X.: Dominant Processes of  
526 HONO Derived from Multiple Field Observations in Contrasting Environments, *Environ. Sci.*  
527 *Technol. Lett.*, 9, 258-264, <https://doi.org/10.1021/acs.estlett.2c00004>, 2022.
- 528 Jiang, Y., Xue, L., Gu, R., Jia, M., Zhang, Y., Wen, L., Zheng, P., Chen, T., Li, H., Shan, Y., Zhao,  
529 Y., Guo, Z., Bi, Y., Liu, H., Ding, A., Zhang, Q., and Wang, W.: Sources of nitrous acid  
530 (HONO) in the upper boundary layer and lower free troposphere of the North China Plain:  
531 insights from the Mount Tai Observatory, *Atmos. Chem. Phys.*, 20, 12115-12131,  
532 <https://doi.org/10.5194/acp-20-12115-2020>, 2020.
- 533 Kasibhatla, P., Sherwen, T., Evans, M. J., Carpenter, L. J., Reed, C., Alexander, B., Chen, Q., Sulprizio,  
534 M. P., Lee, J. D., Read, K. A., Bloss, W., Crilley, L. R., Keene, W. C., Pszenny, A. A. P., and  
535 Hodzic, A.: Global impact of nitrate photolysis in sea-salt aerosol on NO<sub>x</sub>, OH, and O<sub>3</sub> in the  
536 marine boundary layer, *Atmos. Chem. Phys.*, 18, 11185-11203, <https://doi.org/10.5194/acp-18-11185-2018>, 2018.
- 538 Kebede, M. A., Bish, D. L., Losovyj, Y., Engelhard, M. H., and Raff, J. D.: The Role of Iron-Bearing  
539 Minerals in NO<sub>2</sub> to HONO Conversion on Soil Surfaces, *Environ. Sci. Technol.*, 50, 8649-  
540 8660, <https://doi.org/10.1021/acs.est.6b01915>, 2016.
- 541 Kleffmann, J.: Daytime sources of nitrous acid (HONO) in the atmospheric boundary layer,  
542 *Chemphyschem*, 8, 1137-1144, <https://doi.org/10.1002/cphc.200700016>, 2007.
- 543 Kleffmann, J., Becker, K., and Wiesen, P.: Heterogeneous NO<sub>2</sub> conversion processes on acid surfaces:  
544 possible atmospheric implications, *Atmos. Environ.*, 32, 2721-2729,  
545 [https://doi.org/10.1016/S1352-2310\(98\)00065-X](https://doi.org/10.1016/S1352-2310(98)00065-X), 1998.
- 546 Kleffmann, J., Kurtenbach, R., Lörzer, J., Wiesen, P., Kalthoff, N., Vogel, B., and Vogel, H.: Measured  
547 and simulated vertical profiles of nitrous acid—Part I: Field measurements, *Atmos. Environ.*,  
548 37, 2949-2955, [https://doi.org/10.1016/s1352-2310\(03\)00242-5](https://doi.org/10.1016/s1352-2310(03)00242-5), 2003.
- 549 Kleffmann, J., Gavriiloaei, T., Hofzumahaus, A., Holland, F., Koppmann, R., Rupp, L., Schlosser, E.,  
550 Siese, M., and Wahner, A.: Daytime formation of nitrous acid: A major source of OH radicals  
551 in a forest, *Geophys. Res. Lett.*, 32, L05818, <https://doi.org/10.1029/2005gl022524>, 2005.
- 552 Kramer, L. J., Crilley, L. R., Adams, T. J., Ball, S. M., Pope, F. D., and Bloss, W. J.: Nitrous acid  
553 (HONO) emissions under real-world driving conditions from vehicles in a UK road tunnel,  
554 *Atmos. Chem. Phys.*, 20, 5231–5248, <https://doi.org/10.5194/acp-20-5231-2020>, 2020.
- 555 Kurtenbach, R., Becker, K. H., Gomes, J. A. G., Kleffmann, J., Lorzer, J. C., Spittler, M., Wiesen, P.,  
556 Ackermann, R., Geyer, A., and Platt, U.: Investigations of emissions and heterogeneous  
557 formation of HONO in a road traffic tunnel, *Atmos. Environ.*, 35, 3385-3394,  
558 [https://doi.org/10.1016/s1352-2310\(01\)00138-8](https://doi.org/10.1016/s1352-2310(01)00138-8), 2001.
- 559 Lee, J. D., Whalley, L. K., Heard, D. E., Stone, D., Dunmore, R. E., Hamilton, J. F., Young, D. E.,  
560 Allan, J. D., Laufs, S., and Kleffmann, J.: Detailed budget analysis of HONO in central London  
561 reveals a missing daytime source, *Atmos. Chem. Phys.*, 16, 2747-2764,  
562 <https://doi.org/10.5194/acp-16-2747-2016>, 2016.
- 563 Lelièvre, S., Bedjanian, Y., Laverdet, G., and Le Bras, G. : Heterogeneous Reaction of NO<sub>2</sub> with  
564 Hydrocarbon Flame Soot, *J. Phys. Chem. A*, 108, 10807–10817,  
565 <https://doi.org/10.1021/jp0469970>, 2004.
- 566 Li, D., Xue, L., Wen, L., Wang, X., Chen, T., Mellouki, A., Chen, J., and Wang, W.: Characteristics  
567 and sources of nitrous acid in an urban atmosphere of northern China: Results from 1-yr  
568 continuous observations, *Atmos. Environ.*, 182, 296-306,  
569 <https://doi.org/10.1016/j.atmosenv.2018.03.033>, 2018.



- 570 Li, M., Su, H., Li, G., Ma, N., Pöschl, U., and Cheng, Y.: Relative importance of gas uptake on aerosol  
571 and ground surfaces characterized by equivalent uptake coefficients, *Atmos. Chem. Phys.*, 19,  
572 10981-11011, <https://doi.org/10.5194/acp-19-10981-2019>, 2019.
- 573 Liao, S., Zhang, J., Yu, F., Zhu, M., Liu, J., Ou, J., Dong, H., Sha, Q., Zhong, Z., Xie, Y., Luo, H.,  
574 Zhang, L., and Zheng, J.: High Gaseous Nitrous Acid (HONO) Emissions from Light-Duty  
575 Diesel Vehicles, *Environ. Sci. Technol.*, 55, 200-208, <https://doi.org/10.1021/acs.est.0c05599>,  
576 2021.
- 577 Liu, C.-M., Young, C.-Y., and Lee, Y.-C.: Influence of Asian dust storms on air quality in Taiwan,  
578 *Science of The Total Environment*, 368, 884-897,  
579 <https://doi.org/10.1016/j.scitotenv.2006.03.039>, 2006.
- 580 Liu, J., Li, S., Mekic, M., Jiang, H., Zhou, W., Loisel, G., Song, W., Wang, X., and Gligorovski, S.:  
581 Photoenhanced Uptake of NO<sub>2</sub> and HONO Formation on Real Urban Grime, *Environ. Sci.*  
582 *Technol. Lett.*, 6, 413-417, <https://doi.org/10.1021/acs.estlett.9b00308>, 2019a.
- 583 Liu, Y., Shen, H., Mu, J., Li, H., Chen, T., Yang, J., Jiang, Y., Zhu, Y., Meng, H., Dong, C., Wang,  
584 W., and Xue, L.: Formation of peroxyacetyl nitrate (PAN) and its impact on ozone production  
585 in the coastal atmosphere of Qingdao, North China, *Sci. Total Environ.*, 778, 146265,  
586 <https://doi.org/10.1016/j.scitotenv.2021.146265>, 2021.
- 587 Liu, Y. H., Lu, K. D., Li, X., Dong, H. B., Tan, Z. F., Wang, H. C., Zou, Q., Wu, Y. S., Zeng, L. M.,  
588 Hu, M., Min, K. E., Kecorius, S., Wiedensohler, A., and Zhang, Y. H.: A Comprehensive  
589 Model Test of the HONO Sources Constrained to Field Measurements at Rural North China  
590 Plain, *Environ. Sci. Technol.*, 53, 3517-3525, <https://doi.org/10.1021/acs.est.8b06367>, 2019b.
- 591 Meusel, H., Kuhn, U., Reiffs, A., Mallik, C., Harder, H., Martinez, M., Schuladen, J., Bohn, B.,  
592 Parchatka, U., Crowley, J. N., Fischer, H., Tomsche, L., Novelli, A., Hoffmann, T., Janssen, R.  
593 H. H., Hartogensis, O., Pikridas, M., Vrekoussis, M., Bourtsoukidis, E., Weber, B., Lelieveld,  
594 J., Williams, J., Poschl, U., Cheng, Y. F., and Su, H.: Daytime formation of nitrous acid at a  
595 coastal remote site in Cyprus indicating a common ground source of atmospheric HONO and  
596 NO, *Atmos. Chem. Phys.*, 16, 14475-14493, <https://doi.org/10.5194/acp-16-14475-2016>, 2016.
- 597 Nie, W., Ding, A. J., Xie, Y. N., Xu, Z., Mao, H., Kerminen, V. M., Zheng, L. F., Qi, X. M., Huang,  
598 X., Yang, X. Q., Sun, J. N., Herrmann, E., Petäjä, T., Kulmala, M., and Fu, C. B.: Influence of  
599 biomass burning plumes on HONO chemistry in eastern China, *Atmos. Chem. Phys.*, 15, 1147-  
600 1159, <https://doi.org/10.5194/acp-15-1147-2015>, 2015.
- 601 Reed, C., Evans, M. J., Crilley, L. R., Bloss, W. J., Sherwen, T., Read, K. A., Lee, J. D., and Carpenter,  
602 L. J.: Evidence for renoxification in the tropical marine boundary layer, *Atmos. Chem. Phys.*,  
603 17, 4081-4092, <https://doi.org/10.5194/acp-17-4081-2017>, 2017.
- 604 Romer, P. S., Wooldridge, P. J., Crouse, J. D., Kim, M. J., Wennberg, P. O., Dibb, J. E., Scheuer, E.,  
605 Blake, D. R., Meinardi, S., Brosius, A. L., Thames, A. B., Miller, D. O., Brune, W. H., Hall, S.  
606 R., Ryerson, T. B., and Cohen, R. C.: Constraints on Aerosol Nitrate Photolysis as a Potential  
607 Source of HONO and NO<sub>x</sub>, *Environ. Sci. Technol.*, 52, 13738-13746,  
608 <https://doi.org/10.1021/acs.est.8b03861>, 2018.
- 609 Shi, Q., Tao, Y., Krechmer, J. E., Heald, C. L., Murphy, J. G., Kroll, J. H., and Ye, Q.: Laboratory  
610 Investigation of Renoxification from the Photolysis of Inorganic Particulate Nitrate, *Environ.*  
611 *Sci. Technol.*, 55, 854-861, <https://doi.org/10.1021/acs.est.0c06049>, 2021.
- 612 Stemmler, K., Ammann, M., Donders, C., Kleffmann, J., and George, C.: Photosensitized reduction of  
613 nitrogen dioxide on humic acid as a source of nitrous acid, *Nature*, 440, 195-198,  
614 <https://doi.org/10.1038/nature04603>, 2006.
- 615 Stemmler, K., Ndour, M., Elshorbany, Y., Kleffmann, J., D'Anna, B., George, C., Bohn, B., and  
616 Ammann, M.: Light induced conversion of nitrogen dioxide into nitrous acid on submicron  
617 humic acid aerosol, *Atmos. Chem. Phys.*, 7, 4237-4248, <https://doi.org/10.5194/acp-7-4237-2007>,  
618 2007.



- 619 Su, H., Cheng, Y. F., Shao, M., Gao, D. F., Yu, Z. Y., Zeng, L. M., Slanina, J., Zhang, Y. H., and  
620 Wiedensohler, A.: Nitrous acid (HONO) and its daytime sources at a rural site during the 2004  
621 PRIDE-PRD experiment in China, *J. Geophys. Res. Atmos.*, 113,  
622 <https://doi.org/10.1029/2007JD009060>, 2008.
- 623 Su, H., Cheng, Y., Oswald, R., Behrendt, T., Trebs, I., Meixner, F. X., Andreae, M. O., Cheng, P.,  
624 Zhang, Y., and Poschl, U.: Soil nitrite as a source of atmospheric HONO and OH radicals,  
625 *Science*, 333, 1616-1618, <https://doi.org/10.1126/science.1207687>, 2011.
- 626 Tang, Y., An, J., Wang, F., Li, Y., Qu, Y., Chen, Y., and Lin, J.: Impacts of an unknown daytime  
627 HONO source on the mixing ratio and budget of HONO, and hydroxyl, hydroperoxyl, and  
628 organic peroxy radicals, in the coastal regions of China, *Atmos. Chem. Phys.*, 15, 9381-9398,  
629 <https://doi.org/10.5194/acp-15-9381-2015>, 2015.
- 630 Theys, N., Volkamer, R., Müller, J. F., Zarzana, K. J., Kille, N., Clarisse, L., De Smedt, I., Lerot, C.,  
631 Finkenzeller, H., Hendrick, F., Koenig, T. K., Lee, C. F., Knote, C., Yu, H., and Van  
632 Roozendaal, M.: Global nitrous acid emissions and levels of regional oxidants enhanced by  
633 wildfires, *Nat. Geosci.*, 13, 681-686, <https://doi.org/10.1038/s41561-020-0637-7>, 2020.
- 634 Tong, S., Hou, S., Zhang, Y., Chu, B., Liu, Y., He, H., Zhao, P., and Ge, M.: Exploring the nitrous  
635 acid (HONO) formation mechanism in winter Beijing: direct emissions and heterogeneous  
636 production in urban and suburban areas, *Faraday Discuss.*, 189, 213-230,  
637 <https://doi.org/10.1039/c5fd00163c>, 2016.
- 638 Underwood, G. M., Song, C. H., Phadnis, M., Carmichael, G. R., and Grassian, V. H.: Heterogeneous  
639 reactions of NO<sub>2</sub> and HNO<sub>3</sub> on oxides and mineral dust: A combined laboratory and modeling  
640 study, *J. Geophys. Res. Atmos.*, 106, 18055-18066, <https://doi.org/10.1029/2000JD900552>,  
641 2001.
- 642 VandenBoer, T. C., Brown, S. S., Murphy, J. G., Keene, W. C., Young, C. J., Pszenny, A. A. P., Kim,  
643 S., Warneke, C., de Gouw, J. A., Maben, J. R., Wagner, N. L., Riedel, T. P., Thornton, J. A.,  
644 Wolfe, D. E., Dube, W. P., Ozturk, F., Brock, C. A., Grossberg, N., Lefer, B., Lerner, B.,  
645 Middlebrook, A. M., and Roberts, J. M.: Understanding the role of the ground surface in  
646 HONO vertical structure: High resolution vertical profiles during NACHTT-11, *J. Geophys.*  
647 *Res. Atmos.*, 118, 10155-10171, <https://doi.org/10.1002/jgrd.50721>, 2013a.
- 648 VandenBoer, T. C., Brown, S. S., Murphy, J. G., Keene, W. C., Young, C. J., Pszenny, A. A. P., Kim,  
649 S., Warneke, C., de Gouw, J. A., Maben, J. R., Wagner, N. L., Riedel, T. P., Thornton, J. A.,  
650 Wolfe, D. E., Dubé, W. P., Öztürk, F., Brock, C. A., Grossberg, N., Lefer, B., Lerner, B.,  
651 Middlebrook, A. M., and Roberts, J. M.: Understanding the role of the ground surface in  
652 HONO vertical structure: High resolution vertical profiles during NACHTT-11, *J. Geophys.*  
653 *Res. Atmos.*, 118, 10155-110171, <https://doi.org/10.1002/jgrd.50721>, 2013b.
- 654 Villena, G., Wiesen, P., Cantrell, C. A., Flocke, F., Fried, A., Hall, S. R., Hornbrook, R. S., Knapp, D.,  
655 Kosciuch, E., Mauldin, R. L., McGrath, J. A., Montzka, D., Richter, D., Ullmann, K., Walega,  
656 J., Weibring, P., Weinheimer, A., Staebler, R. M., Liao, J., Huey, L. G., and Kleffmann, J.:  
657 Nitrous acid (HONO) during polar spring in Barrow, Alaska: A net source of OH radicals?, *J.*  
658 *Geophys. Res. Atmos.*, 116, D00R07, <https://doi.org/10.1029/2011jd016643>, 2011.
- 659 Vogel, B., Vogel, H., Kleffmann, J., and Kurtenbach, R.: Measured and simulated vertical profiles of  
660 nitrous acid—Part II. Model simulations and indications for a photolytic source, *Atmos.*  
661 *Environ.*, 37, 2957-2966, [https://doi.org/10.1016/s1352-2310\(03\)00243-7](https://doi.org/10.1016/s1352-2310(03)00243-7), 2003.
- 662 Wang, S.: Atmospheric observations of enhanced NO<sub>2</sub>-HONO conversion on mineral dust particles,  
663 *Geophys. Res. Lett.*, 30, <https://doi.org/10.1029/2003gl017014>, 2003.
- 664 Wang, Y. Q.: MeteoInfo: GIS software for meteorological data visualization and analysis, *MeApp*, 21,  
665 360-368, <https://doi.org/10.1002/met.1345>, 2012.
- 666 Wojtal, P., Halla, J. D., and McLaren, R.: Pseudo steady states of HONO measured in the nocturnal  
667 marine boundary layer: a conceptual model for HONO formation on aqueous surfaces, *Atmos.*  
668 *Chem. Phys.*, 11, 3243-3261, <https://doi.org/10.5194/acp-11-3243-2011>, 2011.



- 669 Wu, C., Zhang, S., Wang, G., Lv, S., Li, D., Liu, L., Li, J., Liu, S., Du, W., Meng, J., Qiao, L., Zhou,  
670 M., Huang, C., and Wang, H.: Efficient Heterogeneous Formation of Ammonium Nitrate on  
671 the Saline Mineral Particle Surface in the Atmosphere of East Asia during Dust Storm Periods,  
672 *Environ Sci Technol*, 54, 15622-15630, <https://doi.org/10.1021/acs.est.0c04544>, 2020.
- 673 Xing, L., Wu, J., Elser, M., Tong, S., Liu, S., Li, X., Liu, L., Cao, J., Zhou, J., El-Haddad, I., Huang,  
674 R., Ge, M., Tie, X., Prévôt, A. S. H., and Li, G.: Wintertime secondary organic aerosol  
675 formation in Beijing–Tianjin–Hebei (BTH): contributions of HONO sources and  
676 heterogeneous reactions, *Atmos. Chem. Phys.*, 19, 2343-2359, <https://doi.org/10.5194/acp-19-2343-2019>, 2019.
- 677  
678 Xue, C., Ye, C., Kleffmann, J., Zhang, C., Catoire, V., Bao, F., Mellouki, A., Xue, L., Chen, J., Lu,  
679 K., Zhao, Y., Liu, H., Guo, Z., and Mu, Y.: Atmospheric measurements at Mt. Tai—Part I:  
680 HONO formation and its role in the oxidizing capacity of the upper boundary layer, *Atmos.*  
681 *Chem. Phys.*, 22, 3149-3167, <https://doi.org/10.5194/acp-22-3149-2022>, 2022.
- 682 Xue, C. Y., Zhang, C. L., Ye, C., Liu, P. F., Catoire, V., Krysztofiak, G., Chen, H., Ren, Y. G., Zhao,  
683 X. X., Wang, J. H., Zhang, F., Zhang, C. X., Zhang, J. W., An, J. L., Wang, T., Chen, J. M.,  
684 Kleffmann, J., Mellouki, A., and Mu, Y. J.: HONO Budget and Its Role in Nitrate Formation  
685 in the Rural North China Plain, *Environ. Sci. Technol.*, 54, 11048-11057,  
686 <https://doi.org/10.1021/acs.est.0c01832>, 2020.
- 687 Xue, L. K., Wang, T., Gao, J., Ding, A. J., Zhou, X. H., Blake, D. R., Wang, X. F., Saunders, S. M.,  
688 Fan, S. J., Zuo, H. C., Zhang, Q. Z., and Wang, W. X.: Ground-level ozone in four Chinese  
689 cities: precursors, regional transport and heterogeneous processes, *Atmos. Chem. Phys.*, 14,  
690 13175-13188, <https://doi.org/10.5194/acp-14-13175-2014>, 2014.
- 691 Yang, J., Shen, H., Guo, M.-Z., Zhao, M., Jiang, Y., Chen, T., Liu, Y., Li, H., Zhu, Y., Meng, H.,  
692 Wang, W., and Xue, L.: Strong marine-derived nitrous acid (HONO) production observed in  
693 the coastal atmosphere of northern China, *Atmos. Environ.*, 244, 117948,  
694 <https://doi.org/10.1016/j.atmosenv.2020.117948>, 2021a.
- 695 Yang, Y., Li, X., Zu, K., Lian, C., Chen, S., Dong, H., Feng, M., Liu, H., Liu, J., Lu, K., Lu, S., Ma,  
696 X., Song, D., Wang, W., Yang, S., Yang, X., Yu, X., Zhu, Y., Zeng, L., Tan, Q., and Zhang,  
697 Y.: Elucidating the effect of HONO on O<sub>3</sub> pollution by a case study in southwest China, *Sci.*  
698 *Total Environ.*, 756, 144127, <https://doi.org/10.1016/j.scitotenv.2020.144127>, 2021b.
- 699 Ye, C., Zhang, N., Gao, H., and Zhou, X.: Photolysis of Particulate Nitrate as a Source of HONO and  
700 NO<sub>x</sub>, *Environ. Sci. Technol.*, 51, 6849-6856, <https://doi.org/10.1021/acs.est.7b00387>, 2017.
- 701 Ye, C., Zhou, X., Pu, D., Stutz, J., Festa, J., Spolaor, M., Tsai, C., Cantrell, C., Mauldin, R. L., 3rd,  
702 Campos, T., Weinheimer, A., Hornbrook, R. S., Apel, E. C., Guenther, A., Kaser, L., Yuan, B.,  
703 Karl, T., Haggerty, J., Hall, S., Ullmann, K., Smith, J. N., Ortega, J., and Knote, C.: Rapid  
704 cycling of reactive nitrogen in the marine boundary layer, *Nature*, 532, 489-491,  
705 <https://doi.org/10.1038/nature17195>, 2016a.
- 706 Ye, C. X., Gao, H. L., Zhang, N., and Zhou, X. L.: Photolysis of Nitric Acid and Nitrate on Natural  
707 and Artificial Surfaces, *Environ. Sci. Technol.*, 50, 3530-3536,  
708 <https://doi.org/10.1021/acs.est.5b05032>, 2016b.
- 709 Yu, C., Wang, Z., Ma, Q., Xue, L., George, C., and Wang, T.: Measurement of heterogeneous uptake  
710 of NO<sub>2</sub> on inorganic particles, sea water and urban grime, *J. Environ. Sci.*, 106, 124-135,  
711 <https://doi.org/10.1016/j.jes.2021.01.018>, 2021.
- 712 Yu, C., Huang, L., Xue, L., Shen, H., Li, Z., Zhao, M., Yang, J., Zhang, Y., Li, H., Mu, J., and Wang,  
713 W.: Photoenhanced Heterogeneous Uptake of NO<sub>2</sub> and HONO Formation on Authentic Winter  
714 Time Urban Grime, *ACS Earth Space Chem.*, 6, 1960-1968,  
715 <https://doi.org/10.1021/acsearthspacechem.2c00054>, 2022a.
- 716 Yu, Y., Cheng, P., Li, H., Yang, W., Han, B., Song, W., Hu, W., Wang, X., Yuan, B., Shao, M., Huang,  
717 Z., Li, Z., Zheng, J., Wang, H., and Yu, X.: Budget of nitrous acid (HONO) at an urban site in

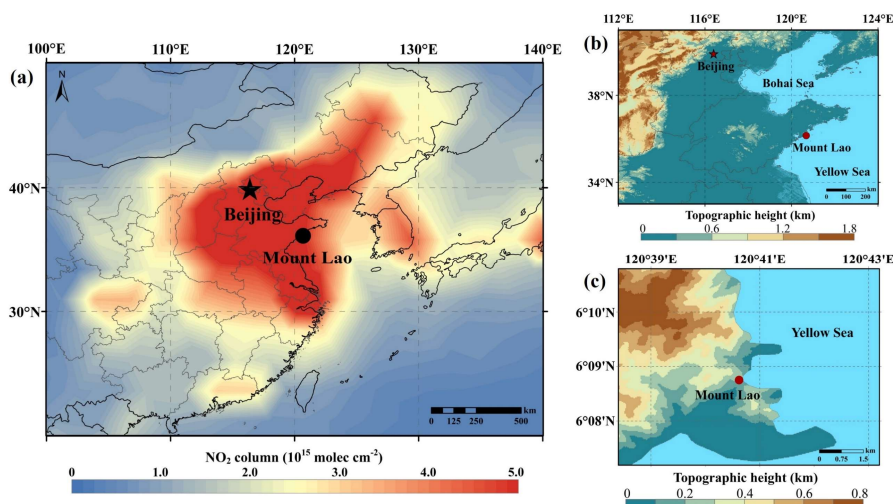


- 718 the fall season of Guangzhou, China, *Atmos. Chem. Phys.*, 22, 8951-8971,  
719 <https://doi.org/10.5194/acp-22-8951-2022>, 2022b.
- 720 Zha, Q. Z., Xue, L. K., Wang, T., Xu, Z., Yeung, C. P., Louie, P. K. K., and Luk, C. W. Y.: Large  
721 conversion rates of NO<sub>2</sub> to HNO<sub>2</sub> observed in air masses from the South China Sea: Evidence  
722 of strong production at sea surface?, *Geophys. Res. Lett.*, 41, 7710-7715,  
723 <https://doi.org/10.1002/2014gl061429>, 2014.
- 724 Zhang, R., Gen, M., Huang, D., Li, Y., and Chan, C. K.: Enhanced Sulfate Production by Nitrate  
725 Photolysis in the Presence of Halide Ions in Atmospheric Particles, *Environ. Sci. Technol.*, 54,  
726 3831-3839, <https://doi.org/10.1021/acs.est.9b06445>, 2020.
- 727 Zhang, W., Tong, S., Ge, M., An, J., Shi, Z., Hou, S., Xia, K., Qu, Y., Zhang, H., Chu, B., Sun, Y.,  
728 and He, H.: Variations and sources of nitrous acid (HONO) during a severe pollution episode  
729 in Beijing in winter 2016, *Sci. Total Environ.*, 648, 253-262,  
730 <https://doi.org/10.1016/j.scitotenv.2018.08.133>, 2019.
- 731 Zhou, X., Zhang, N., TerAvest, M., Tang, D., Hou, J., Bertman, S., Alaghmand, M., Shepson, P. B.,  
732 Carroll, M. A., Griffith, S., Dusanter, S., and Stevens, P. S.: Nitric acid photolysis on forest  
733 canopy surface as a source for tropospheric nitrous acid, *Nat. Geosci.*, 4, 440-443,  
734 <https://doi.org/10.1038/ngeo1164>, 2011.
- 735 Zhou, X. L., Gao, H. L., He, Y., Huang, G., Bertman, S. B., Civerolo, K., and Schwab, J.: Nitric acid  
736 photolysis on surfaces in low-NO<sub>x</sub> environments: Significant atmospheric implications,  
737 *Geophys. Res. Lett.*, 30, <https://doi.org/10.1029/2003gl018620>, 2003.
- 738 Zhu, Y., Wang, Y., Zhou, X., Elshorbany, Y. F., Ye, C., Hayden, M., and Peters, A. J.: An investigation  
739 into the chemistry of HONO in the marine boundary layer at Tudor Hill Marine Atmospheric  
740 Observatory in Bermuda, *Atmos. Chem. Phys.*, 22, 6327-6346, <https://doi.org/10.5194/acp-22-6327-2022>, 2022.
- 741  
742  
743



744 **Figures and Tables**

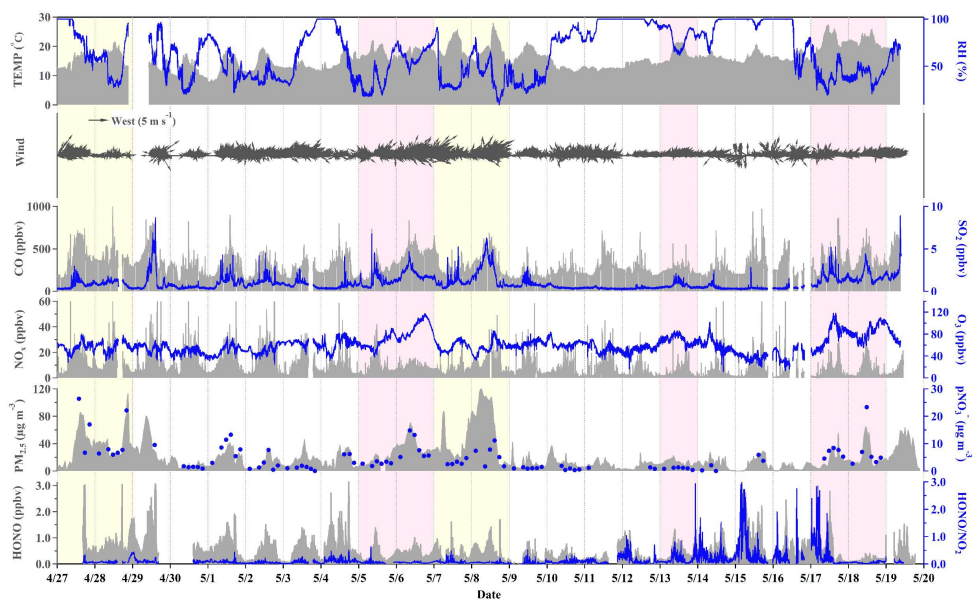
745



746

747 **Figure 1.** Maps showing the location of the monitoring site. Figure 1a is colored by tropospheric NO<sub>2</sub>  
748 column density in May 2021 from the Ozone Monitoring Instrument (OMI,  
749 <https://www.earthdata.nasa.gov/>), and Figure 1b and Figure 1c are colored by the geographical height  
750 from the Geospatial Data Cloud (<http://www.gscloud.cn/>).

751

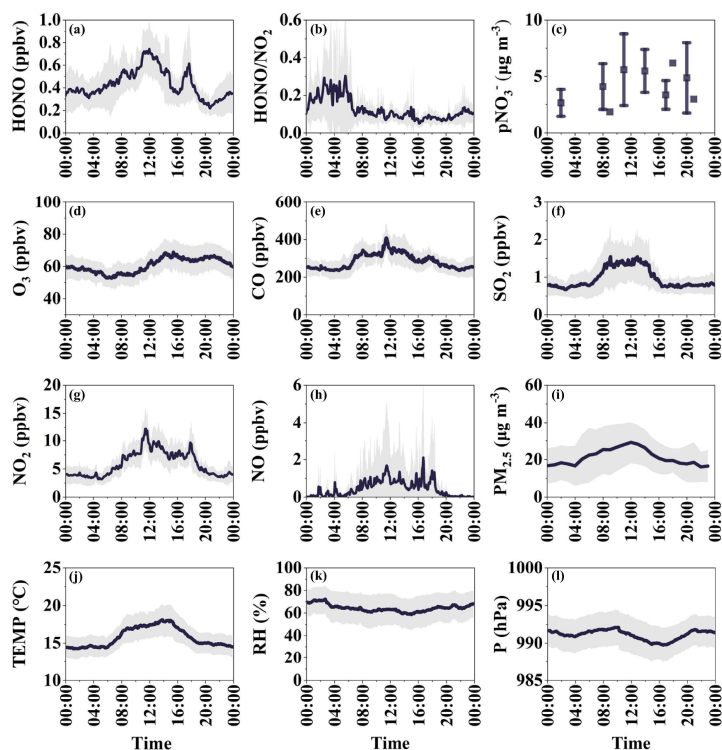


752

753 **Figure 2.** Time series of HONO, meteorological parameters, and related species measured during the  
754 campaign. The yellow shaded areas correspond to the period of dust, while the pink shaded areas  
755 represent the period of photochemical pollution.

756

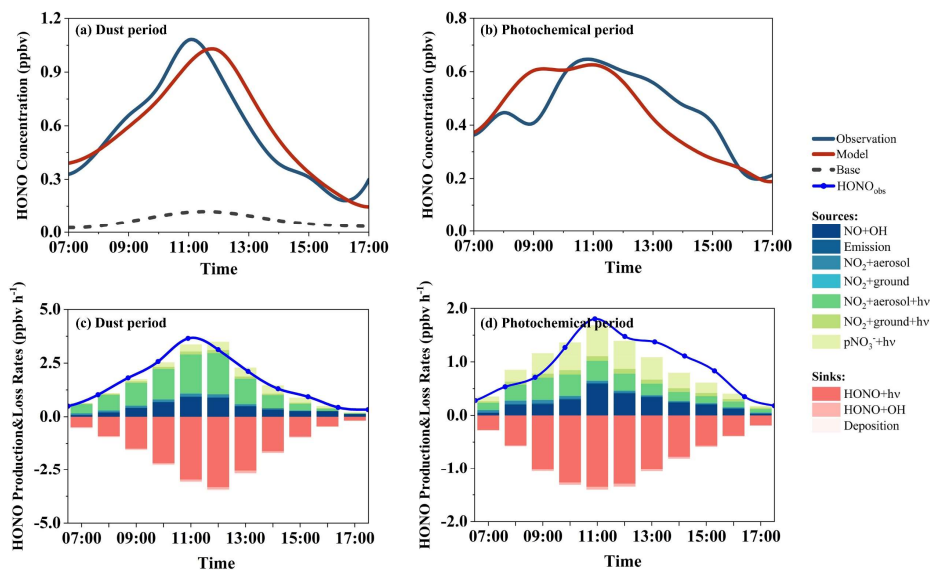




757

758 **Figure 3.** Average diurnal variations of (a) HONO, (b) HONO/NO<sub>2</sub>, (c) particle nitrate, (d) O<sub>3</sub>, (e) CO,  
 759 (f) SO<sub>2</sub>, (g) NO<sub>2</sub>, (h) NO, (i) PM<sub>2.5</sub>, (j) temperature, (k) RH, and (l) pressure during the observation  
 760 period. The shaded area indicates the range of half of the standard deviation.

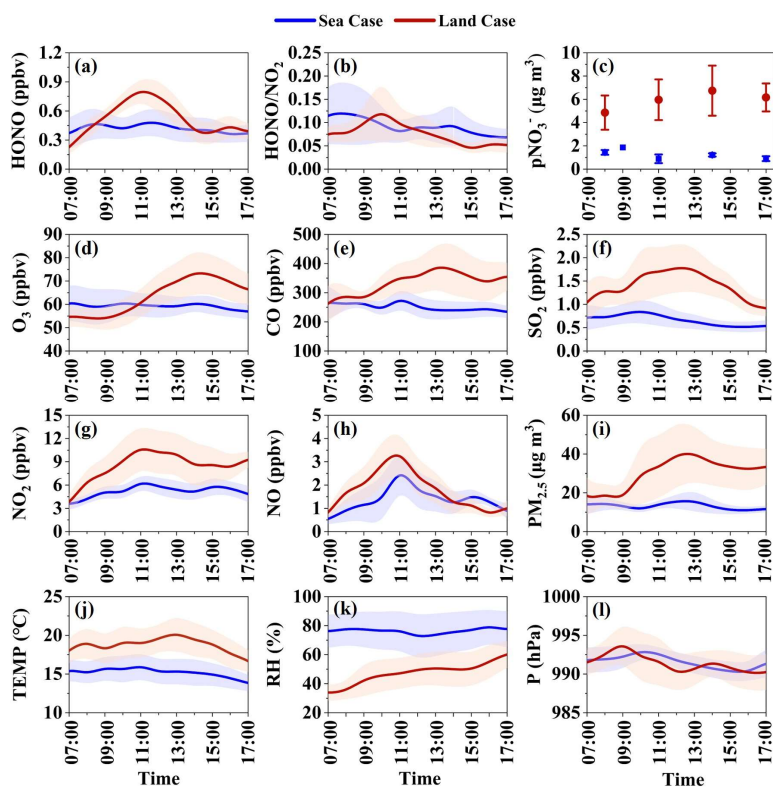
761



762

763 **Figure 4.** Daytime HONO budgets in dust (a, c) and (b, d) photochemical period at Mount Lao. The  
 764 base case only considered the homogeneous reaction of NO + OH, and the model case considered the  
 765 updated HONO sources described in this study.

766

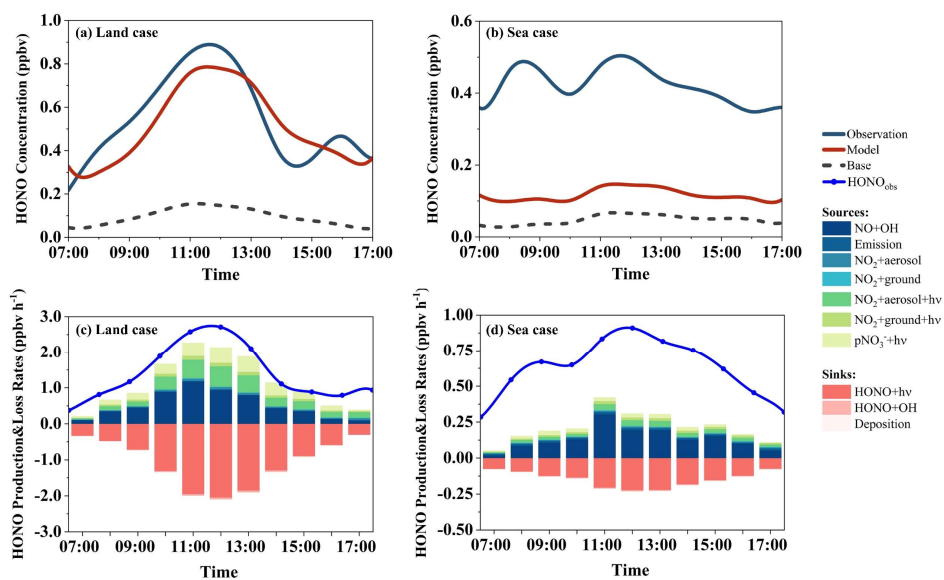


767

768 **Figure 5.** Average diurnal variations of HONO and related parameters in the “sea case” and the “land

769 case” during the campaign at Mount Lao. The shaded area indicates half of the standard deviation.

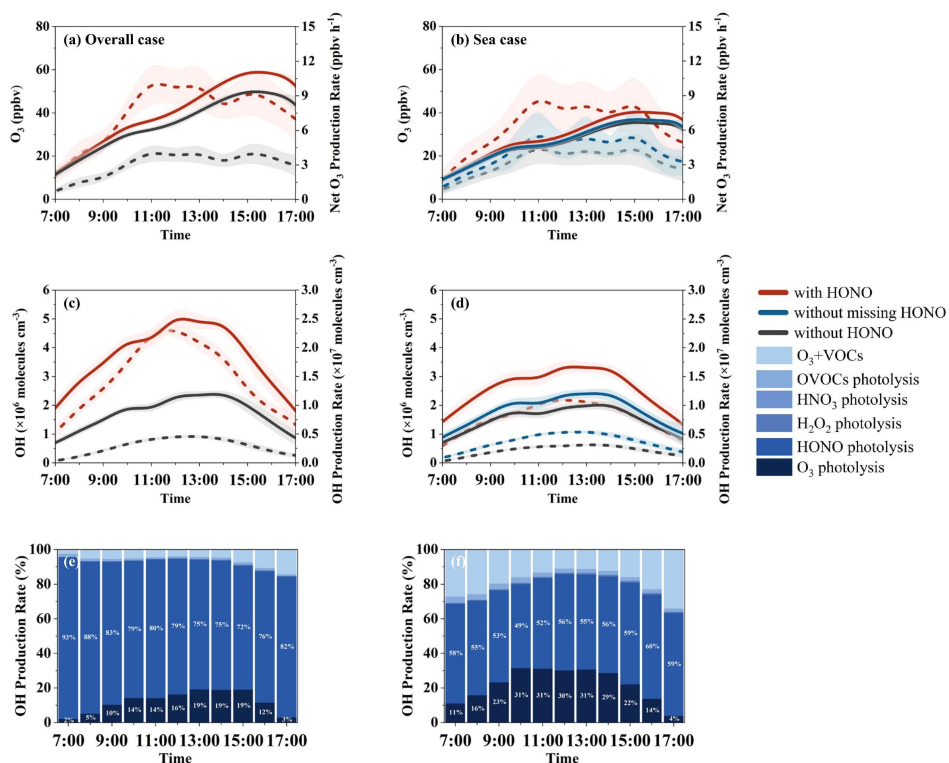
770



771

772 **Figure 6.** Comparison of the observed and modeled daytime (7:00–17:00) HONO concentrations and  
773 modeled HONO budgets in the “land case” (a, c) and the “sea case” (b, d).

774



775

776 **Figure 7.** Comparison of simulated O<sub>3</sub> and OH radical concentration (solid lines) and production rate  
 777 (dashed lines) with and without HONO measurement data constraints and relative diurnal  
 778 contributions of different OH radical sources with HONO constrained in the “land case” (a, c, e) and  
 779 the “sea case” (b, d, f). The shaded area indicates the standard deviation.

780



781 **Table 1.** Summary of HONO source and sinks included in the box model.

Pathways	Parametrization	References
Direct emission	$k_{\text{emission}} = 0.8\%$	Kleffmann et al. (2003)
$\text{OH} + \text{NO} \rightarrow \text{HONO}$	$k_{\text{OH+NO}}$	Calculated in model
$\text{NO}_2 + \text{H}_2\text{O} \xrightarrow{\text{aerosol surface}} \text{HONO} + \text{HNO}_3$	$k = 0.25 \times v_{\text{NO}_2} \times \text{Sa} \times \gamma_a$ $\gamma_a = 8 \times 10^{-6}$	Vandenboer et al. (2013a)
$\text{NO}_2 + \text{H}_2\text{O} \xrightarrow{\text{ground surface}} \text{HONO} + \text{HNO}_3$	$k = 0.25 \times v_{\text{NO}_2} \times \gamma_g \times \frac{S}{V}$ $\gamma_g = 1 \times 10^{-6}, \frac{S}{V} = \frac{1.7}{\text{BLH}}$	Kleffmann et al. (1998); Vogel et al. (2003)
$\text{NO}_2 + h\nu \xrightarrow{\text{aerosol surface}} \text{HONO}$	$k = 0.25 \times v_{\text{NO}_2} \times \text{Sa} \times \gamma_{a, h\nu} \times \frac{J_{\text{NO}_2}}{J_{\text{NO}_2, \text{noon}}}$ $\gamma_{a, h\nu} = 4 \times 10^{-5}$	Lelièvre et al. (2004)
$\text{NO}_2 + h\nu \xrightarrow{\text{ground surface}} \text{HONO}$	$k = 0.25 \times v_{\text{NO}_2} \times \gamma_{g, h\nu} \times \frac{S}{V} \times \frac{J_{\text{NO}_2}}{J_{\text{NO}_2, \text{noon}}}$ $\gamma_{g, h\nu} = 2 \times 10^{-5}, \frac{S}{V} = \frac{1.7}{\text{BLH}}$	Stemmler et al. (2006); Vogel et al. (2003)
$\text{pNO}_3^- + h\nu \rightarrow \text{HONO}$	$k = \frac{8.3 \times 10^{-5}}{7 \times 10^{-7}} \times J(\text{HNO}_3)_{\text{MCM}}$	Ye et al. (2017)
$\text{HONO} + h\nu \rightarrow \text{NO} + \text{OH}$	$k = J(\text{HONO})$	Calculated in model
$\text{HONO} + \text{OH} \rightarrow \text{H}_2\text{O} + \text{NO}_2$	$k_{\text{OH+HONO}}$	Calculated in model
Deposition	$k = \frac{v_{\text{HONO}}}{\text{BLH}}$	Calculated in model

782



783 **Table 2.** Statistics of measured species and meteorological parameters during the campaign.

Parameters	Mean	SD	Minimum	Median	Maximum
HONO (ppbv)	0.46	0.37	< DL (0.005)	0.38	3.14
HONO/NO <sub>2</sub>	0.13	0.24	–	0.07	2.97
NO (ppbv)	0.9	1.7	0.1	0.2	38.3
NO <sub>2</sub> (ppbv)	5.9	4.8	0.4	4.6	65.1
O <sub>3</sub> (ppbv)	60.4	15.8	11.6	58.8	118.1
CO (ppbv)	284.0	118.8	104.2	250.3	1046.7
SO <sub>2</sub> (ppbv)	1.0	0.8	< DL (0.12)	0.7	8.9
PM <sub>2.5</sub> (µg m <sup>-3</sup> )	21.2	21.0	< DL (0.5)	14.4	120.7
Sa (m <sup>2</sup> m <sup>-3</sup> )	6.2×10 <sup>-4</sup>	5.8×10 <sup>-4</sup>	2.8×10 <sup>-4</sup>	4.2×10 <sup>-4</sup>	3.1×10 <sup>-3</sup>
pNO <sub>3</sub> <sup>-</sup> (µg m <sup>-3</sup> )	4.6	5.0	0.02*	2.8	26.4
TEMP (°C)	15.1	3.4	7.5	15.6	27.9
RH (%)	68.7	26.1	9.0	64.8	99.9
P (kPa)	991.1	4.4	979.0	991.0	1003.0
WS (m s <sup>-1</sup> )	1.23	0.96	0*	1.00	9.30
WD (°)	–	–	0	247	354

784 DL: detection limit.

785



786 **Table 3.** Comparison of the statistics for the measured species and meteorological parameters during  
 787 dust, photochemical pollution, and non-polluted periods in the daytime (7:00–17:00).

Parameters	Dust period	Photochemical period	Non-polluted period
HONO (ppbv)	0.57 ± 0.39	0.44 ± 0.29	0.40 ± 0.34
HONO/NO <sub>2</sub>	0.07 ± 0.04	0.10 ± 0.13	0.10 ± 0.12
NO (ppbv)	1.8 ± 1.8	1.2 ± 1.4	1.8 ± 2.0
NO <sub>2</sub> (ppbv)	9.8 ± 5.0	7.1 ± 4.4	7.1 ± 4.6
O <sub>3</sub> (ppbv)	58.0 ± 10.8	78.8 ± 17.3	54.9 ± 11.7
CO (ppbv)	371.8 ± 151.9	353.8 ± 117.5	277.6 ± 98.0
SO <sub>2</sub> (ppbv)	1.6 ± 1.3	1.7 ± 0.8	0.7 ± 0.6
PM <sub>2.5</sub> (µg m <sup>-3</sup> )	45.4 ± 32.3	25.0 ± 17.4	17.2 ± 12.6
PM <sub>10</sub> (µg m <sup>-3</sup> )	235.3 ± 200.8	68.0 ± 47.2	32.8 ± 21.8
Sa (m <sup>2</sup> m <sup>-3</sup> )	1.28 × 10 <sup>-3</sup> ± 8.41 × 10 <sup>-4</sup>	6.81 × 10 <sup>-4</sup> ± 4.73 × 10 <sup>-4</sup>	5.58 × 10 <sup>-4</sup> ± 4.22 × 10 <sup>-4</sup>
pNO <sub>3</sub> <sup>-</sup> (µg m <sup>-3</sup> )	7.0 ± 6.2	6.2 ± 5.6	3.0 ± 3.4
TEMP (°C)	19.0 ± 3.4	20.5 ± 2.7	15.1 ± 2.4
RH (%)	47.8 ± 24.7	47.4 ± 17.2	71.6 ± 27.0
WS (m s <sup>-1</sup> )	0.42 ± 0.35	0.65 ± 0.33	0.38 ± 0.25
JNO <sub>2</sub> (s <sup>-1</sup> )	6.6 × 10 <sup>-3</sup> ± 2.2 × 10 <sup>-3</sup>	7.0 × 10 <sup>-3</sup> ± 2.1 × 10 <sup>-3</sup>	4.5 × 10 <sup>-3</sup> ± 2.2 × 10 <sup>-3</sup>

788